UNIVERSIDADE FEDERAL DE PERNAMBUCO
CENTRO DE CIÊNCIAS EXATAS E DA NATUREZA
PROGRAMA DE PÓS-GRADUAÇÃO EM FÍSICA

Rafael Magalhães Jungmann

STATE DEPENDENT COMPLEXITY OF LOCAL FIELD POTENTIALS IN THE PRIMARY VISUAL CORTEX

Recife

2024

Rafael Magalhães Jungmann

STATE DEPENDENT COMPLEXITY OF LOCAL FIELD POTENTIALS IN THE PRIMARY VISUAL CORTEX

Tese apresentada ao Programa de Pós-Graduação em Física da Universidade Federal de Pernambuco, como requisito parcial para a obtenção do título de Doutor em Física.

Área de Concentração: Dinâmica Não-Linear, Caos e Sistemas Complexos

Orientador (a): Prof. Dr. Pedro Valadão Carelli

Coorientador (a): Prof. Dr. Nivaldo Antônio Portela de Vasconcelos

Recife

2024

.Catalogação de Publicação na Fonte. UFPE - Biblioteca Central

Jungmann, Rafael Magalhães.
State dependent complexity of local field potentials in the primary visual cortex / Rafael Magalhaes Jungmann. - Recife, 2024.
77f.: il.

Tese (Doutorado) - Universidade Federal de Pernambuco, Centro de Ciências Exatas e da Natureza, Programa de Pós-Graduação em Física, 2024.
Orientação: Pedro Valadão Carelli.
Coorientação: Nivaldo Antônio Portela de Vasconcelos.
Inclui referências.

1. LFP; 2. Estado cortical; 3. Complexidade estatística; 4. Variabilidade de disparo. I. Carelli, Pedro Valadão. II. Vasconcelos, Nivaldo Antônio Portela de. III. Título.

UFPE-Biblioteca Central

RAFAEL MAGALHÃES JUNGMANN

STATE DEPENDENT COMPLEXITY OF LOCAL FIELD POTENTIALS IN THE PRIMARY VISUAL CORTEX

Tese apresentada ao Programa de Pós-Graduação em Física da Universidade Federal de Pernambuco, como requisito parcial para a obtenção do título de Doutor em Física.

Área de Concentração: Dinâmica Não-linear, Caos e Sistemas Complexos

Data de aprovação: 02/12/2024.

BANCA EXAMINADORA

_____
Prof. Dr. Pedro Valadão Carelli
Orientador
Universidade Federal de Pernambuco

_____
Prof. Dr. Clécio Clemente de Souza Silva
Examinador Interno
Universidade Federal de Pernambuco

_____
Prof. Dr. Eduardo Padrón Hernández
Examinador Interno
Universidade Federal de Pernambuco

_____
Prof. Dr. Marcelo Bussotti Reyes
Examinador Externo
Universidade Federal do ABC

_____
Prof. Dr. Tiago Lins Ribeiro
Examinador Externo
National Institute of Mental Health

This thesis is dedicated to my loving parents, whose unwavering support and sacrifices have shaped my journey.

ACKNOWLEDGEMENTS

We thank Conselho Nacional de Desenvolvimento Científico e Tecnológico (CNPq) for finnacial support via grant 314092/2021-8. We thank the Physics Departament of the Federal University of Pernambuco (UFPE-DF) for structural and academic support.

We thank Dr. Fernanda S. Matias and Dr. Mauro Copelli for collaboration and insightful discussions. We thank Dr. Thaís Feliciano, Dr. Leandro A. A. Aguiar, Dr. Ana João Rodrigues, Dr. Carina Soares-Cunha, and Dr. Bárbara Coimbra for providing experimental data from anesthetized rats. We thank Dr. G. Buzsáki, Dr. Y. Senzai and Dr. P. Petersen for the sharing and support of freely moving mice data.

"As long as our brain is a mystery, the universe, the reflection of the structure of the brain will also be a mystery." (Santiago Ramón y Cajal).

RESUMO

O potencial de campo local (LFP) captura a atividade elétrica combinada dos neurônios em uma região do tecido cerebral. Embora amplamente utilizado para estudar ritmos cerebrais e circuitos neurais, a relação precisa entre os LFPs e a atividade de disparo de neurônios ainda é pouco compreendida, especialmente no que diz respeito ao estado cortical. Utilizando uma representação simbólica baseada na técnica de Bandt-Pompe, este trabalho preenche essa lacuna ao encontrar relações consistentes entre o estado cortical, representado pelo coeficiente de variação (CV) da atividade de disparo, e os quantificadores de teoria da informação—entropia de Shannon e complexidade estatística—de dados de LFP obtidos de ratos anestesiados com uretana e camundongos em movimento livre. Nossos resultados demonstram que a complexidade estatística e a entropia de Shannon dos LFPs nas camadas profundas do córtex visual primário (V1) variam consistentemente com a variabilidade de disparo dos neurônios. Exploramos ainda esses quantificadores ao longo das camadas corticais no V1, mostrando que a complexidade estatística é sensível à profundidade, atingindo seu pico na metade da camada 5 à medida que o CV aumenta. Além disso, mostramos que a complexidade estatística dos LFPs varia entre diferentes estados comportamentais dos camundongos em movimento livre.

Palavras-chaves: LFP, estado cortical, complexidade estatística, variabilidade de disparo.

ABSTRACT

The Local field potential (LFP) captures the combined electric activity of neurons in a region of brain tissue. Although widely used to study brain rhythms and neural circuits, the precise relationship between LFPs and spiking activity remains poorly understood, in particular, regarding cortical state. Using a symbolic representation based on Bandt-Pompe technique, this work bridges that gap by finding consistent relations between cortical state, as proxied by the coefficient of variation (CV) of spiking activity and information-theory quantifiers-Shannon entropy and statistical complexity—of LFP data from urethane-anesthetized rats and freely moving mice. Our findings demonstrate that LFP's statistical complexity and Shannon entropy in the deep layers of the primary visual cortex (V1) vary consistently with spiking variability. We further explored these quantifiers across cortical layers in V1, showing that statistical complexity is sensitive to depth, peaking in mid-layer 5 as CV increases. Additionally, we show LFP's statistical complexity varies across behavioral states of freely moving mice.

Keywords: LFP, cortical state, statistical complexity, spiking variability.

LIST OF FIGURES

CONTENTS

1 INTRODUCTION

When one considers the nature of the mind, it's natural to try to relate this to the body's central nervous system and its principal cells, the neurons. This association arise because, in modern science, there is no doubt that synapses between neurons are the foundation of perception, memory, cognitive thinking, motor control, and virtually all other brain functions, concepts introduced even at elementary school levels. However, this was not always the case, in fact, until the end of the 17th century, it was commonly thought, even by prominent thinkers like René Descartes, that the mind was separate from the body, dwelling within an individual's soul. It was only in the early 1800s that biologists like Franz Joseph Gall began to establish the brain as the organ of the mind, with distinct mental functions attributed from different brain regions.

In the 21st century, we have developed state-of-the-art electrophysiology methods to measure the electrical activity of neurons within living brain tissue. Although we still cannot explain how consciousness arises from the brain, we are convinced that the answer lies in the language of electrical signaling between neurons—specifically, the action potential. When a neuron receives sufficient input, it depolarizes and fires an action potential, or spike, transmitting information to other neurons through synaptic connections. This spiking activity is fundamental to processing sensory inputs, driving motor actions, and supporting higher cognitive functions. For this reason, electrophysiology has been one of the central focuses of modern neuroscience.

The history of brain electrophysiology began in the late 18th century with the pioneering work of Luigi Galvani, who discovered that electrical stimulation could cause muscle contractions. His experiments on frogs led to the theory of "animal electricity," sparking early investigations into the role of electricity in the nervous system. This discovery laid the groundwork for studying bioelectric phenomena in the brain and nervous system, suggesting that the brain itself might function through electrical signals. In the 19th century, scientists like Richard Caton and Emil du Bois-Reymond made significant advances in brain electrophysiology. In 1875, Caton was the first to observe electrical activity in the brain using a galvanometer to record oscillations from the cerebral cortex of animals. Around the same time, du Bois-Reymond's work on action potentials demonstrated that electrical impulses were integral to nerve and muscle function, reinforcing the idea that electrical signals were a key aspect of brain communication. Their work paved the way for more precise measurements of electrical

activity in the brain.

The 20th century saw major breakthroughs in electrophysiology with Hans Berger's invention of the electroencephalogram (EEG) in 1924, a device that could noninvasively record the brain's electrical activity from the scalp. Berger's recordings revealed rhythmic patterns of brain activity, including the well-known alpha waves (7-12 Hz) observed during relaxed wakefulness. His work provided a tool that allowed researchers to study brain rhythms in humans and animals, leading to the identification of various brain wave patterns associated with different states of consciousness, such as sleep, alertness, and epilepsy. In the latter half of the 20th century and into the 21st, advancements in electrophysiological techniques expanded researchers' ability to explore brain activity in more detail. Technologies like magnetoencephalography (MEG) and intracranial EEG, known as electrocorticogram (ECoG) and local field potential (LFP), as well as computational models of neural dynamics, have enabled researchers to study both the macroscopic and microscopic electrical activity in the brain. These advancements have contributed to a deeper understanding of brain functions like cognition, sensory processing, and motor control, while also aiding in the diagnosis and treatment of neurological disorders.

Also in the 20th century, intracellular measurements of neuronal electrical dynamics began, particularly in the late 1930s when Kenneth S. Cole and Howard Curtis developed techniques to measure the electrical properties of cell membranes. They pioneered the use of glass microelectrodes, which could penetrate a neuron's membrane to record its voltage from inside the cell. This marked a major advancement over previous techniques that could only measure extracellular potentials. Cole and Curtis were the first to document significant changes in membrane resistance during an action potential, suggesting that ions were flowing through channels in the membrane. However, the mechanisms behind this process were not understood until the early 1950s, when Alan Hodgkin, Andrew Huxley, and Bernard Katz, building on Cole and Curtis' work, performed the first precise intracellular measurements of membrane potential in the squid giant axon. Using voltage-clamp technique, they were able to control the neuron's membrane potential and measure the ionic currents that generate the action potential (see Fig. 2(a)). Their experiments revealed the roles of sodium and potassium ions in the action potential and led to the formulation of the Hodgkin-Huxley model, which quantitatively described the ionic basis of neuronal excitability, earning them the Nobel Prize in 1963.

While studies of the intracellular electrical dynamics of isolated neurons have driven the whole field of spiking activity of neuron populations, extracellular recording methods, like EEG and LFP, continue to be researched, as they provide a more holistic view of the brain activity,

encompassing all forms of interactions between neurons and brain tissue. But what exactly does all these technologies measure? What are the main differences between them?

Electroencephalography (EEG), electrocorticography (ECoG), magnetoencephalography (MEG), and local field potentials (LFP) are all techniques used to study summed electrical activity of the brain, but they differ in how they capture electrical signals and in their level of spatial and temporal resolution. EEG is a noninvasive method that measures electrical activity by placing electrodes on the scalp, integrating areas of 10 cm^2 or more, providing a global overview of brain activity. This technique is particularly useful for studying general brain rhythms and detecting abnormalities like seizures. However, EEG has relatively low spatial resolution and it produces a very noisy signal due to skull and scalp interference; nonetheless, it has high temporal resolution, capturing changes in brain activity within milliseconds. ECoG, on the other hand, involves placing platinum–iridium or stainless steel electrodes underneath the skull directly on the surface of the brain (cerebral cortex), offering much higher spatial resolution ($< mm^2$) than EEG by using flexible, closely spaced subdural grid or strip electrodes closer to the source. However, a craniotomy (the removal of the skull bone) is required for the recording; nevertheless, it is still used in clinical settings, often for epilepsy surgery. MEG measures the magnetic fields generated by neural electrical activity using highly sensitive magnetometers placed outside the head. Like EEG, it is noninvasive and offers excellent temporal resolution, but MEG has superior spatial resolution compared to EEG because magnetic fields are less distorted by the skull. LFPs, in contrast, are usually recorded with multi-electrode silicon probes, at a very high recording rate, implanted directly into brain tissue, capturing the summed electrical activity of neurons in a localized area. LFPs provide the finest spatial resolution of the four, allowing for detailed studies of neural circuits.

Examples of these different recording methods are provided in Fig. 1, taken from (BUZSÁKI; ANASTASSIOU; KOCH, 2012). In Fig. 1(a), we see extracellular traces using different recording methods, specifically, recordings of LFP from two selected sites of three electrodes in the left amygdala and hippocampus, ECoG recordings from three different regions, a 3×8 subdural grid electrode array placed over the lateral left temporal cortex, two four-contact strips placed under the inferior temporal surface, an eight-contact strip placed over the left orbitofrontal surface, and EEG over both hemispheres on the frontal and occipital lobes (Fz and O_2 sites). Note that the amplitude of the signals are larger and the higher-frequency patterns have greater resolution at the intracerebral (LFP) and ECoG sites compared to scalp EEG. Fig. 1(b) shows 6-second traces of slow waves recorded by EEG (Cz, red), and LFP (blue) recorded by

Figure 1 – Extracellular traces using various recording methods.(a) Simultaneous recordings of local field potential (LFP) from three depth electrodes (two selected sites each) in the left amygdala and hippocampus, electrocorticogram (ECoG) recording from three different regions, a 3×8 subdural grid electrode array placed over the lateral left temporal cortex, two four-contact strips placed under the inferior temporal surface, an eight-contact strip placed over the left orbitofrontal surface, and scalp electroencephalography (EEG) over both hemispheres (selected sites are the Fz and O_2) in a patient with drug-resistant epilepsy.(b) 6s traces of slow waves recorded by scalp EEG (Cz, red), and LFP (blue) recorded by electrodes placed in the deep layers of the supplementary motor area (SM), entorhinal cortex (EC), hippocampus (HC), and amygdala (Am). Also shown are population firing rates (green) and spikes of isolated neurons (black ticks). (c) Simultaneously recorded magnetoencephalogram (MEG; black) and anterior hippocampus depth EEG (red) from a patient with drug-resistant epilepsy.(d) Simultaneously recorded LFP traces from the superficial and deep layers of the motor cortex in an anaesthetized cat and an intracellular trace from a layer 5 pyramidal neuron.

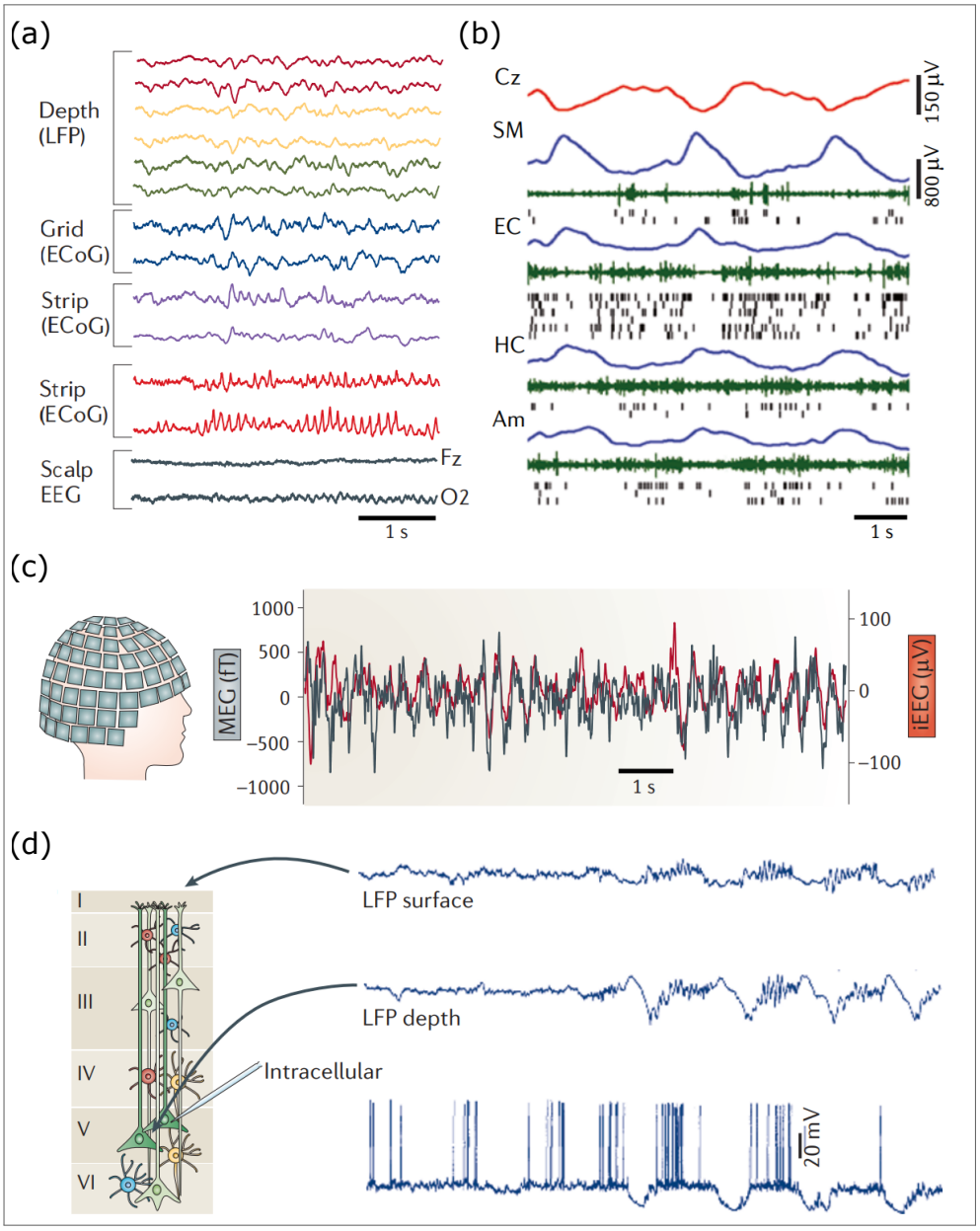

Source: from BUZSÁKI; ANASTASSIOU; KOCH (2012)

electrodes placed in deep layers of the supplementary motor area (SM), entorhinal cortex (EC), hippocampus (HC), and amygdala (Am), along with population spiking activity (green) and spikes from isolated neurons (black ticks). Fig. 1(c) shows simultaneously recorded MEG (black) and anterior hippocampus depth EEG (red) from a patient with drug-resistant epilepsy. Note the similar oscillations recorded by the depth electrode and the trace calculated by the MEG, with no phase delay. Fig. 1(d) shows recorded LFP traces from the superficial and deep layers of the motor cortex in an anesthetized cat along with an intracellular trace from a layer 5 pyramidal neuron of the cortex. Note the alternation of hyperpolarization and depolarization (slow oscillation) of the layer 5 neuron and the corresponding changes in the LFP.

We see from Fig. 1(d) that there is an underlying connection between the LFP and the intracellular recording, specifically during bursts of rapid, transient electrical impulses generated by the neuron. This phenomenon is referred to as spiking activity and reflects the temporal recordings of action potentials or spikes, which are fundamental to neural communication. The pattern and frequency of spiking activity carry important information about the neuron's role in a network, with neurons often firing in synchrony or in rhythmic patterns, reflecting how the brain encodes information. Studying these patterns allows researchers to understand how neural circuits perform computations and how information is represented and transmitted across different brain regions. The spike patterns from single neurons can be measured from intracellular recordings, as shown in Fig. 2(a). However, when analyzing a neuron population, it's experimentally unviable to simultaneously record intracellular potentials from hundreds of neurons with traditional glass microelectrodes, especially *in vivo* for long periods of time (several seconds). This is straightforward in simulations of neuron models, where each cell's potential can be tracked separately in conjunction with the global activity of the neurons, as seen in Fig. 2(c). A way to mitigate this is by taking advantage of the fast-recording multi-electrode probes used to track extracellular potentials, such as LFPs, through a process called spike sorting, where spikes from individual neurons can be obtained from the unfiltered data from the probes. This allows long periods of spiking activity of neuron populations to be experimentally measured, which is ideal for studying spiking patterns and how they change across different brain regions.

Notably, the technological advancement of simultaneous recording techniques for large neuronal populations (NICOLELIS et al., 2003; CSICSVARI et al., 2003; STEVENSON; KORDING, 2011; JUN et al., 2017) has revolutionized our understanding of the dynamics of the cerebral cortex, particularly the variability of spiking activity in several cortical areas, including the

Figure 2 – Recordings of action potentials in both experimental and simulation levels. (a) First published intracellular recording of an action potential, recorded in 1939 by Hodgkin and Huxley from a squid giant axon, using glass capillary electrodes filled with sea water. Pulses are separated by 2 ms and vertical scale indicates the potential of the internal electrode in mV.(b) Intracellular recording of the membrane potential, where multiple action potentials, or spikes, can be tracked as the fast bursts of amplitudes.(c) Simulations of spiking activity of neuron models. The top panel shows a raster diagram of the activity of 250 neurons from the simulation, and the the bottom panel is the membrane voltage of a single randomly chosen neuron.

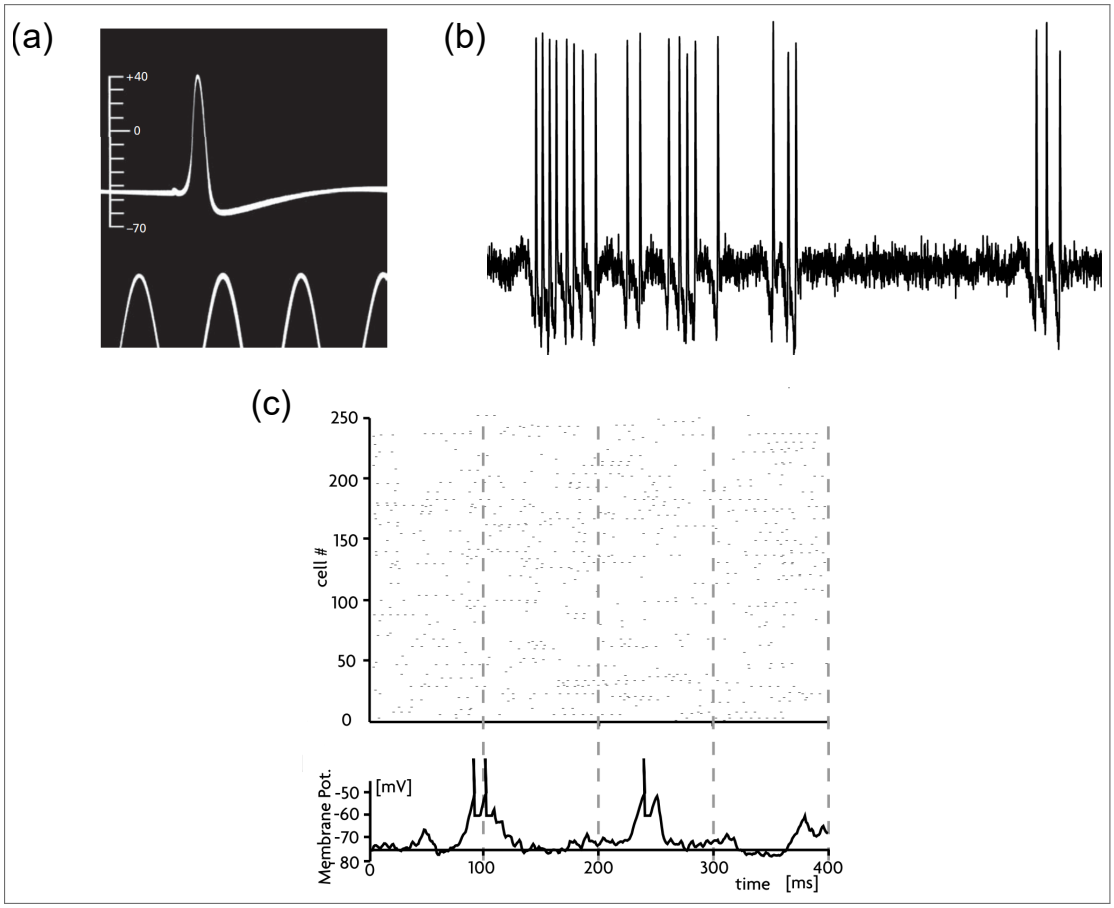

Source: adapted from KANDEL (2013) , VOGELS; ABBOTT (2005) , and neuwritewest.org

primary visual cortex, where cortical neurons exhibit remarkable variability in their spiking patterns (SHADLEN; NEWSOME, 1998). This spiking variability during spontaneous activity (in the absence of induced sensory stimulation) exhibits similarities to the spiking activity triggered by stimuli in freely moving animals (TSODYKS et al., 1999; RINGACH, 2009).

Spiking variability in primary sensory cortices varies across different cortical states, which are characterized by varying levels of neural synchronization (RENART et al., 2010; HARRIS; THIELE, 2011; MCGINLEY et al., 2015; SCHÖLVINCK et al., 2015). Cortical states refer to the overall dynamics of activity within the cerebral cortex, influenced by the balance of excitatory and inhibitory inputs as well as global factors like attention, arousal, and external stimuli. These states can dramatically affect spiking activity. For example, in an active, awake state, the cortex

often exhibits desynchronized activity with a mix of high-frequency, irregular spiking patterns that facilitate flexible processing of information. In contrast, during sleep or states of deep anesthesia, cortical activity tends to be more synchronized, dominated by slow-wave oscillations with lower-frequency spiking. These shifts in cortical states reflect different functional modes of the brain, ranging from high-level cognitive processing in awake states to the consolidation of memories during sleep.

Spiking activity and cortical states are tightly linked and dynamically modulate one another. Changes in cortical states can alter how neurons spike and how networks process information, while spiking activity, in turn, can influence cortical state transitions. For example, during attention or task engagement, neurons may shift to more precise, coordinated spiking patterns, enhancing the brain's ability to filter and process relevant information. Similarly, bursts of synchronized spiking during slow-wave sleep may contribute to memory consolidation. This suggests that spiking variability can serve as a proxy for cortical state at both macro and microscopic scales. This variability appears to be a dynamic property, changing over time on a timescale of seconds. Therefore, investigating the state dependence of cortical functions is fundamental for understanding the intricate mechanisms underlying cortical computations and their modulation by multiple behavioral factors.

The power spectrum of combined electrophysiological activity in the cortical extracellular medium typically exhibits a $1/f$ structure, characterized by elevated power in lower-frequency (below 10 Hz) components (HENRIE; SHAPLEY, 2005; BUZSÁKI; ANASTASSIOU; KOCH, 2012). These components primarily reflect the concerted local activity of neural networks, which occurs within a restricted volume of tissue surrounding the electrode tip (BUZSÁKI; ANASTASSIOU; KOCH, 2012). The use of extracellular signals, in particular, of LFP to assess the overall neural function within a specific tissue area is gaining increasing attention (PESARAN et al., 2018; EINEVOLL et al., 2013; RIMEHAUG et al., 2023). LFP is mainly believed to reflect the synaptic currents of neuron populations in the vicinity of the recording site, making them sensitive to the geometry and arrangement of the neurons (HERRERAS, 2016). However, any transmembrane current in the brain tissue contributes to the LFP, which complicates the interpretation of the signal's precise origin and spatial reach (KATZNER et al., 2009; LINDÉN et al., 2011; KAJIKAWA; SCHROEDER, 2011). Despite this challenge, analyzing LFP signals is essential to understanding both presynaptic and postsynaptic activity and inferring properties of network dynamics. However, there is a lack of studies regarding the complexity of LFP signals along different cortical states, particularly in the sensory areas.

To address this issue, we conducted analysis on simultaneous recordings of large neuronal populations in the primary visual cortex, under multiple experimental conditions: deep layers of urethane-anesthetized rats and all layers of freely moving mice. Based on these data, segmented by the level of variability in spiking activity of neuronal populations, we employ two quantifiers from Information Theory: Shannon entropy and MPR-statistical complexity. The latter is based on the disequilibrium between the actual time series and one with a uniform probability distribution function (SHANNON; WEAVER, 1949; LAMBERTI et al., 2004; ROSSO et al., 2007; ZUNINO; SORIANO; ROSSO, 2012; XIONG et al., 2020; LóPEZ-RUIZ; MANCINI; CALBET, 1995). We assign each system under study with a position in a two-dimensional space spanned by the entropy and statistical complexity measure. These quantifiers are evaluated using the probability distribution function (PDF) obtained through the Bandt-Pompe symbolization methodology (BANDT; POMPE, 2002).

Statistical complexity is an entropy-based quantifier that provides a framework for quantifying patterns and structures in data. This makes it a valuable tool for neuroscience, where brain activity exhibits highly dynamic and complex behaviors. One of its primary applications in neuroscience is the analysis of time series data, such as EEG, MEG, and LFP recordings. These datasets often contain nonlinear and non-stationary features, rendering traditional linear models inadequate for fully capturing the brain's intricate dynamics. To analyze these time series from an entropy perspective, the Bandt-Pompe technique must be implemented to capture the probabilistic aspects of the data. More specifically, this technique derives a probability distribution function (PDF) by counting the different ways in which the series change along a given axis.

This approach was originally introduced to distinguish chaotic from stochastic systems in time series analysis (ROSSO et al., 2007). In that work, O. A. Rosso *et al.* computed the statistical complexity (C) and entropy (H) for different chaotic systems and stochastic processes under a set of parameters, presenting the results in a complexity-entropy plane. They concluded that different dynamical systems occupy different locations on the plane, with chaotic systems having a very high statistical complexity and intermediate entropy, as shown in Fig. 3(a). They also found that stochastic processes achieved lower complexity, as more noise was incorporated, while noiseless systems with regular oscillations also displayed lower complexity.

In neuroscience, statistical complexity has recently been applied to various brain signals, for instance, Fig. 3(b) illustrates that the statistical complexity of EEG can be computed, with different stages of EEG recordings during epileptic seizures episodes positioned at distinct

points of the complexity-entropy plane. This indicates that statistical complexity can serve as a marker of EEG states (ROSSO et al., 2006). This framework has also been used to demonstrate that complexity is maximized near criticality in cortical states when using spiking data (LOTFI et al., 2021). It has also been applied to different neuronal signals, such as MEG data (MENDOZA-RUIZ et al., 2020), as well as neuronal activity (MONTANI et al., 2015; MONTANI; DELEGLISE; ROSSO, 2014; LUISE et al., 2021). Furthermore, it has been utilized to analyze monkey LFP to estimate response-related differences between Go and No-Go trials (LUCAS et al., 2021), asses time differences during phase synchronization (MONTANI et al., 2015), and to explore Hénon maps as a model for brain dynamics based on LFP data from the subthalamic nucleus (STN) and medial frontal cortex (MFC) of human patients (GUISANDE et al., 2023).

Figure 3 – Statistical complexity of dynamical systems, where continuous lines are the curves of minimum and maximum complexity and the area enclosed by them is the complexity-entropy ($C - H$) plane.(a) Localization of different chaotic systems and stochastic processes under different parameters (top), and enlargement of right-side of the plane (bottom). Different dynamical systems are placed on different planar locations.(b) Statistical complexity of different stages of EEG recordings of epileptic seizures episodes can be placed at different points of the plane (top), and movement from the points in the plane in 40 seconds periods (bottom).

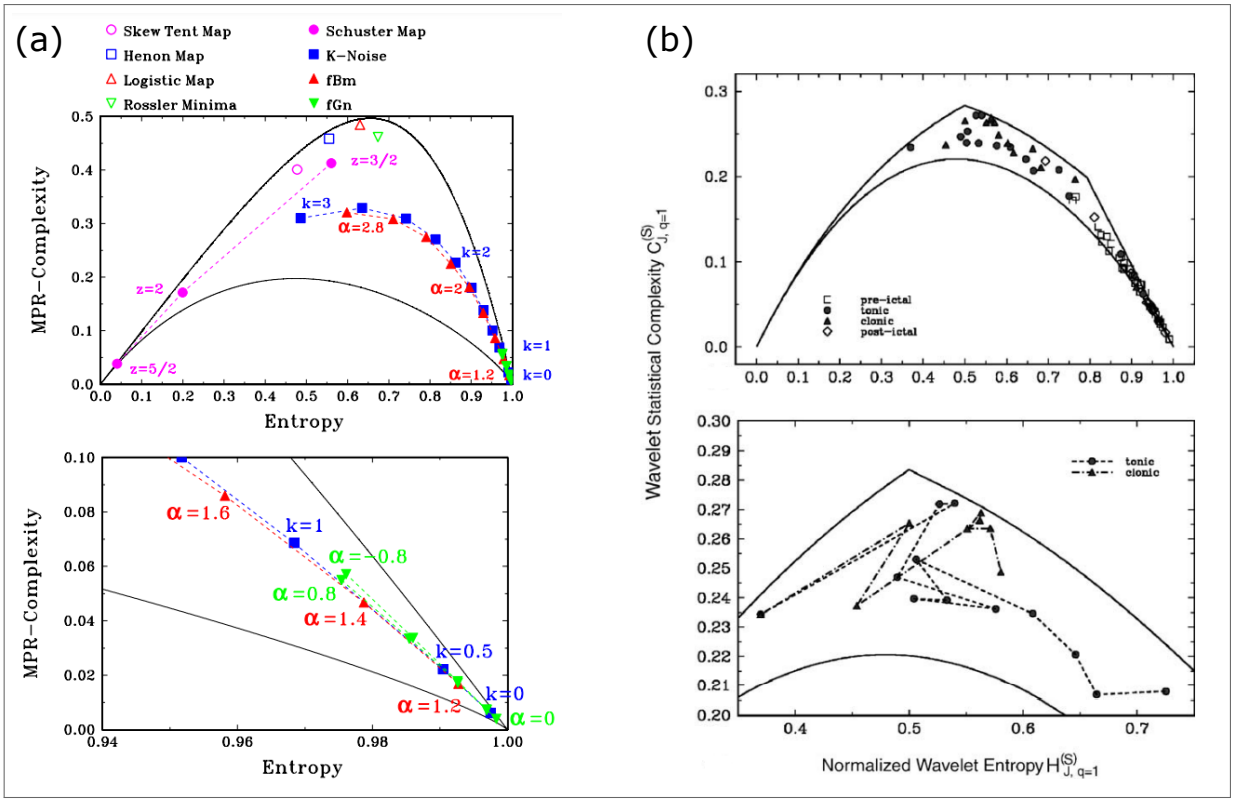

Source: adapted from ROSSO et al. (2006) and ROSSO et al. (2007)

This study utilized this approach to calculate the statistical complexity of local field potential (LFP) data recorded from the deep layers of the primary visual cortex of anesthetized

rats. We segmented the data by cortical state derived from spiking activity and found consistent relationships between spiking variability and the complexity of the LFP. Additionally, we analyzed the statistical complexity of LFPs in mice across different cortical layers, revealing surprising results related to the anatomical structure under various cortical and behavioral states (JUNGMANN et al., 2024).

This thesis will be organized as follows: Chapter 2 will cover the fundamentals of neuronal signals, specifically spiking activity and local field potential, as well as the data acquisition and analysis methods used in this work. In Chapter 3, we will provide an overview of statistical complexity as an information quantifier, along with its applications in neuroscience. Chapter 4 will present and discuss the results of our analysis, and finally, Chapter 5 will summarize the main conclusions of this work and outline future perspectives.

2 NEURONAL SIGNALS AND ANALYSIS

2.1 NERVE CELLS AND ACTION POTENTIALS

The central nervous system (CNS) is responsible for regulating all the autonomic mechanisms essential to bodily functions, such as muscle control required for breathing and digestion. But how can a single system communicate with so many different parts of the body and regulate such a variety of functions? The answer lies in the universal language used by CNS cells, particularly neurons.

The nervous system is made up of two types of cells: nerve cells, known as neurons, and glial cells, known as glia. Neurons are the primary signaling units of the CNS and are responsible for receiving and processing stimuli from the environment, transmitting and filtering information across different regions of the nervous system, and initiating actions in various body systems. Neurons accomplish this by converting any form of stimulus into electrical impulses, which can travel from one neuron to another either through direct electrical currents (creating electrical synapses) or, more commonly, by releasing chemical substances called neurotransmitters, which generate chemical synapses.

Glial cells are known for their supportive role in the nervous system. Unlike neurons, they do not generate electrical impulses; instead, their primary function is to maintain the overall health and functionality of the nervous system. There are several types of glia (e.g., astrocytes, oligodendrocytes), each defined by specific functions and locations within the system. These functions are crucial for neuronal activity, as they help create a suitable environment for neurons, maintain the brain's physical structure, aid in tissue repair and scarring, provide immune responses within the CNS, and ensure efficient signal transmission over long distances.

Because glial cells work behind the scenes, they are often overshadowed by neurons, even though, depending on the region, they are far more numerous—comprising about 50–90% of cells in the human brain. It is important to note that modern research has shown glial cells actively contribute to regulating synaptic activity, forming neural circuits, and even supporting plasticity (SANCHO, 2021), indicating that future biophysical models of neural circuits should consider glial cells as active elements of the system.

2.1.1 Neurons morphology

Neurons are specialized cells in the nervous system responsible for transmitting information throughout the body. They communicate with each other through electrical impulses and chemical signals, known as action potentials and synapses, which utilize the unique structures and connections of neurons. These cells are essential for brain function, controlling everything from muscle movement to thought processes.

A typical neuron has four main regions: the soma, dendrites, axon, and axon terminals. The soma, or cell body, is the metabolic center of the cell, producing neurotransmitters and proteins necessary for function. It also houses the nucleus, where the cell's genetic information is stored. Dendrites are branched, tree-like extensions from the soma that receive incoming signals from other neurons and transmit electrical impulses toward the cell body. The soma integrates these impulses and, if they are strong enough, initiates an action potential, which then travels from the soma down the axon to the axon terminals. The axon, another extension from the soma, varies in length from 0.1 mm to 2 m. At its end, the axon branches into multiple terminals; if an action potential reaches a terminal, it triggers the release of neurotransmitters into the synaptic cleft—the extracellular space between the axon terminal and the target cell membrane. This junction, which includes the axon terminal, synaptic cleft, and postsynaptic membrane, is called a synapse. An illustration of the basic morphology of a neuron is given in Fig. 4(a), however, it should be noted that this representation is generalized and does not capture the diverse branching architectures of dendrites and axons. In the 19th century, Ramón y Cajal examined the structure of neurons in almost every region of the nervous system, identifying that neuron types are distinguished primarily by their form, specifically by the number and structure of processes extending from the soma. Neurons are therefore classified as unipolar, bipolar, or multipolar.

Unipolar neurons, as represented in Fig. 4(b) predominate in the nervous systems of invertebrates and have a single primary process, which usually gives rise to other branches, with one branch serving as the axon and the other branches as the dendrites. Bipolar cells have an oval soma from which two processes emerge, a dendritic structure that receives signals from the periphery of the cell body and an axon that carries information toward the central nervous system, as such, cells related to sensory stimulus are usually bipolar, like those in the retina, shown in Fig. 4(c), and in the olfactory epithelium of the nose. Multipolar neurons, the most common type in vertebrate nervous systems, generally possess a single axon and

multiple dendrites extending from various points around the soma. This type varies widely in shape, particularly in axon length and the size, extent, and complexity of dendritic branching. The extent of dendritic branching correlates with the number of synaptic inputs, ranging from thousands to millions. Fig. 4(a) and (d) are both representations of multipolar neurons, with the first being a spinal motor neuron, and the latter being a pyramidal neuron (named after the triangular shaped soma) of the hippocampus, also typically found in the cerebral cortex.

Figure 4 – Illustration of neurons morphology and classification.(a) Four main morphological regions of a typical motor neuron in the spinal chord: the dendrites, the soma (cell body), the axon and the axon terminals.(b) Unipolar cells from invertebrates have a single process emanating from the cell. Different segments serve as dendritic surfaces or axon terminals. (c) Bipolar cells (from the retina as example) have two types of processes that are functionally distinct, the dendrite that receives electrical signals and the axon transmits signals to other cells. (d) Pyramidal cells, as examples of multipolar cells, have a triangular cell body with dendrites emerging from both the apex (the apical dendrite) and the base (the basal dendrites). Pyramidal cells are found in the hippocampus and throughout the cerebral cortex.

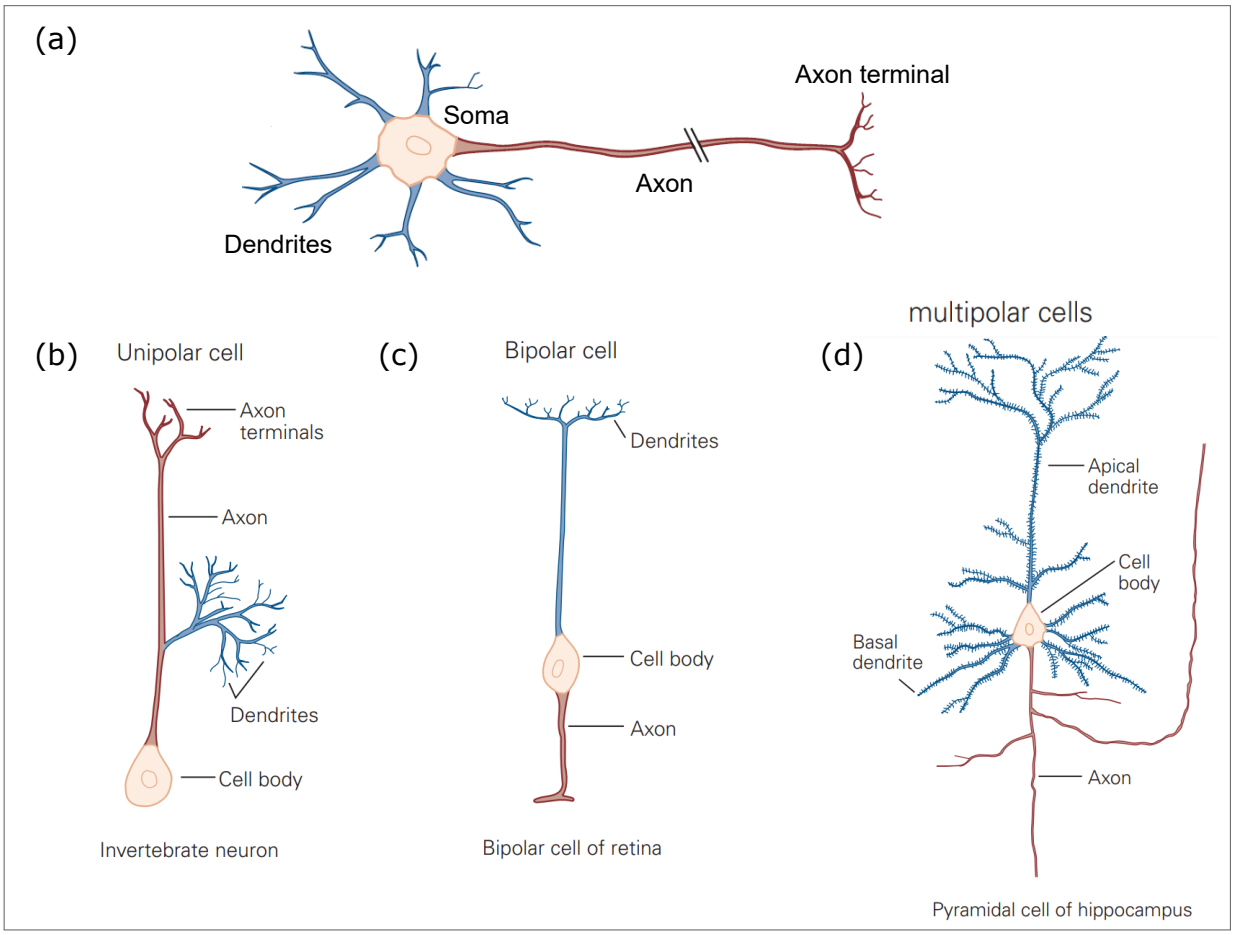

Source: adapted from KANDEL (2013)

Neurons are also classified by their functions as sensory neurons, motor neurons, and interneurons. Sensory neurons transmit information from peripheral sensors in the body to the nervous system, supporting both perception and motor coordination. Some sensory neurons

are referred to as afferent neurons, with the term "afferent" used to describe all information reaching the central nervous system from the periphery, regardless of whether it leads to perception. Typically, the term "sensory neurons" is reserved for afferent inputs that result in perception. Motor neurons, often called efferent neurons, carry commands from the brain or spinal cord to muscles and glands. Interneurons are the most numerous type of neuron and are further divided into two categories: relay and local. Relay, or projection, interneurons have long axons and transmit signals over greater distances, such as from the thalamus to the cortex. Local interneurons, on the other hand, have short axons and form connections with nearby neurons in local circuits. Each of these functional types of neurons can be further subdivided; for example, sensory neurons can be classified according to the type of sensory stimuli to which they respond. These classifications can then be refined further by characteristics such as location, density, and size. For instance, retinal ganglion cells, which respond to light, are divided into 13 types based on their dendritic tree size, branching density, and depth within specific retinal layers.

2.1.2 Ion channels

Figure 5 – Two different types of stimulus controlling the opening and closing of ion channels. (a) Ligand-gated channels open when a type of ligand binds to the external surface of the channel through a receptor site. The energy release from the binding drives the channel to an open state. (b) Voltage-gated channels open and close with changes in the potential gradient across the membrane.

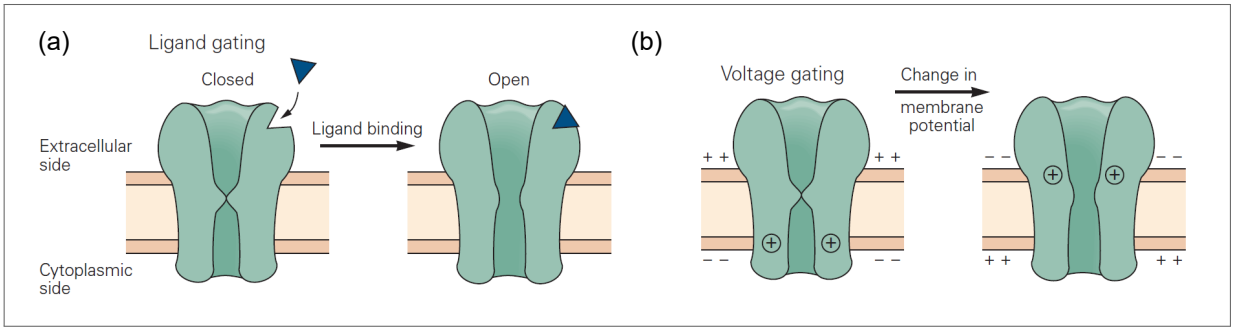

Source: adapted from KANDEL (2013)

We have emphasized that neurons transmit electrical impulses and chemical signals between each other, but how do they accomplish this? Neurons are both electrically and chemically excitable due to specialized proteins in their cell membranes, namely ion channels and receptors. These proteins facilitate the flow of specific inorganic ions, redistributing charge and generating electrical currents that alter the voltage across the membrane.

Ion channels are specialized proteins embedded in the membranes of neurons, and they are critical for transmitting electrical signals throughout the nervous system. These channels selectively allow ions such as sodium (Na^+), potassium (K^+), calcium (Ca^{2+}), and chloride (Cl^-) to pass through the neuronal membrane, creating rapid changes in the cell's electrical potential of up to 500 volts per second. Neurons rely on these changes in ion flow to generate and propagate action potentials, which serve as the primary means of communication within the nervous system. Ion channels possess three main properties: they recognize and select specific ions that can traverse them, open and close in response to specific stimuli, and conduct ions in and out of the neuronal membrane at extremely rapid rates. Depending on the type of channel, up to 100 million ions can pass through each second.

Ion channels open and close in response to specific stimuli, such as voltage changes across the membrane (voltage-gated ion channels), the binding of neurotransmitters (ligand-gated ion channels), or mechanical forces (mechanosensitive channels). When a channel is closed, ions cannot enter or leave the cell because the lipids in the cell membrane are hydrophobic, meaning they do not mix with water. Since the ions are hydrophilic, they attract water and become engulfed in it, which prevents their passage through the membrane. When the channels are open, electrical and diffusion gradients drive specific ions to balance these gradients. For example, Na^+ is much more abundant in the extracellular space than in the intracellular soma, creating a diffusion gradient. As we will discuss further, the membrane's electric potential at rest is negative compared to the extracellular environment. This means that when ion channels selective for Na^+ open, a strong driving force causes Na^+ to flow into the cell through the channel. These electrical and chemical gradients are maintained by ion transporters and pumps, such as the sodium-potassium pump. These proteins do not participate in rapid neuronal signaling but instead establish and maintain the concentration gradients of physiologically important ions between the inside and outside of the cell.

Ion channels are classified not only by their selective ions but also by the stimuli required to open and close them. Voltage-gated channels are those that open or close in response to changes in the electrical potential of the neuron's membrane; an illustration of this is provided in Fig 5(b). The most well-known types of these channels are the voltage-gated sodium and potassium channels, which, as will be discussed later, are essential for generating action potentials. When voltage-gated sodium channels open, allowing Na^+ to rush into the cell, the cell experiences a depolarization, which triggers adjacent sodium channels to drive even more Na^+ into the cell. Following this, voltage-gated potassium channels open to allow

K^+ to exit the cell, as there is a higher concentration of K^+ inside of the cell compared to outside. This repolarizes the membrane and restores the neuron to its resting state. This rapid exchange of ions across the membrane is essential for the neuron's ability to fire repeatedly and efficiently.

In addition to voltage-gated channels, other types of ion channels play crucial roles in neuronal function. Ligand-gated ion channels, as shown in Fig. 5(a), are located at synapses and open in response to neurotransmitter binding, facilitating communication between neurons. When neurotransmitters such as glutamate, GABA, or acetylcholine bind to the receptor site on the ion channel, they induce a conformational change that opens the channel, allowing specific ions associated with that channel to flow into or out of the neuron. This ion movement alters the electric potential of the neuron's membrane, potentially leading to the opening of voltage-gated channels, depending on the ions involved. For example, glutamate typically activates excitatory ligand-gated ion channels, promoting depolarization and the opening of voltage-gated Na^+ channels, while GABA activates inhibitory channels, resulting in hyperpolarization and the opening of Cl^- channels. These channels form the basis of neural communication and plasticity, making them vital for synaptic transmission and enabling the conversion of chemical signals back into electrical signals in postsynaptic neurons.

2.1.3 Action Potential

Information from neurons to their target cells is conveyed by transient electrochemical signals, which are produced by temporary changes in the electric current flowing into and out of the presynaptic neuron. These currents drive the membrane potential away from its resting value.

The neuron's cell membrane has clouds of positive and negative ions distributed across the intracellular and extracellular sides of its surface. At rest, the extracellular region has an excess of positive ions, while the intracellular region has an excess of negative ions. This electrical gradient is maintained by the lipid bilayer of the membrane, which forms a barrier to the diffusion of ions. This separation of charges gives rise to a voltage across the membrane called the *membrane potential* (V_m), defined as

$$V_m = V_{in} - V_{out}, \tag{2.1}$$

where V_{in} and V_{out} are the potential inside and outside of the cell, respectively. The membrane potential at rest is called the resting membrane potential, and, since the potential outside the cell is defined as zero by convention, the membrane potential is equal to V_{in}, which typically ranges from $-60mV$ to $-70mV$. An illustration of the separation of charges in the cell membrane is given in Fig. 6.

Figure 6 – Illustration of the separation of charges at the surface of the cell membrane. The lipid layers in the membrane prevents the diffusion of the ions, resulting in a difference of electric potential, defined as the membrane potential V_m.

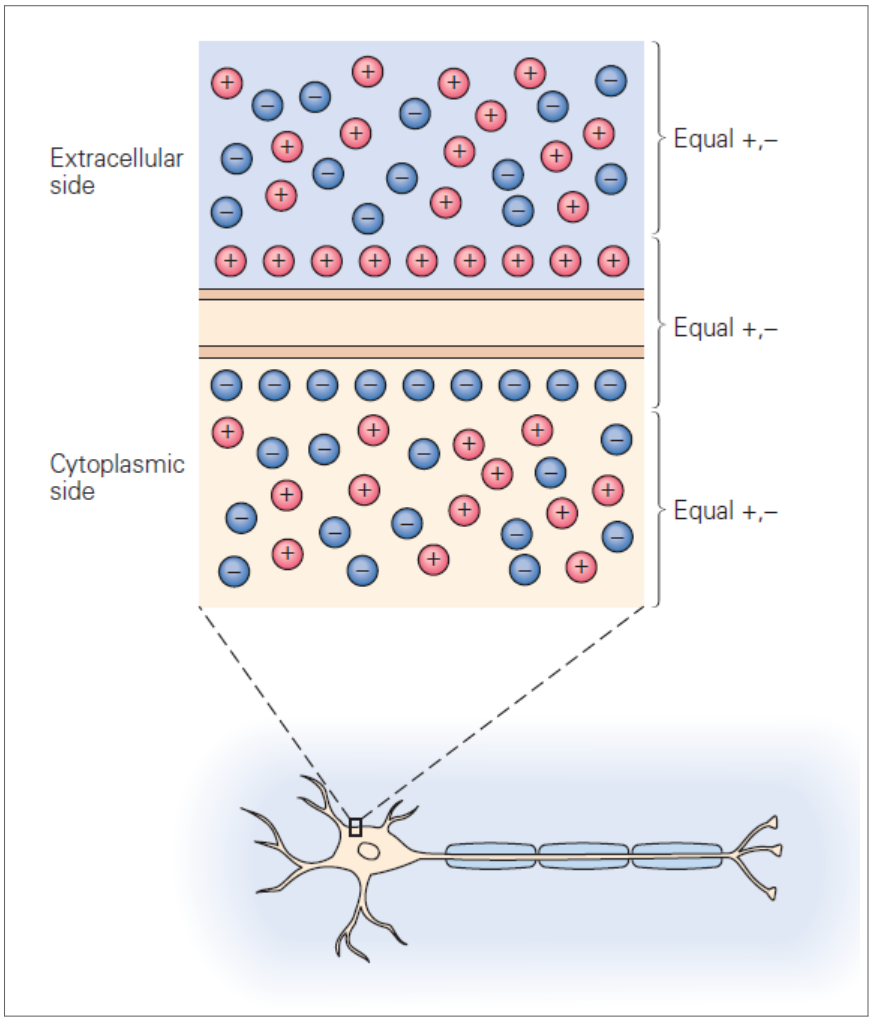

Source: adapted from KANDEL (2013)

The cell's resting state is primarily maintained by non-gated ion channels and sodium-potassium pumps, which ensure that there is a higher concentration of sodium ions outside the cell and a higher concentration of potassium ions inside the cell. However, when a neuron is stimulated by synaptic input or other triggers, voltage-gated sodium (Na^+) channels open, allowing Na^+ ions to flow into the neuron. The influx of positive ions results in a more positive membrane potential, a process known as depolarization. Small depolarizations are typically

followed by the closing of sodium channels, and the membrane potential resets to its resting state through the action of pumps and non-gated potassium channels. If depolarization reaches a certain threshold, usually around $-55mV$,additional sodium channels open, leading to a rapid influx of sodium and a corresponding rapid rise in the membrane potential, which peaks around $+40mV$. Once this peak is reached, the voltage-gated sodium channels are closed, and voltage-gated potassium (K^+) channels open, resulting in an efflux of positive ions that drives the membrane potential back toward its resting value, a process called repolarization. The potassium channels, however, remain open for a short time after repolarization, causing the membrane potential to become more negative than the resting membrane potential, a process known as hyperpolarization.

During the repolarization phase, after the peak of the action potential, the voltage-gated sodium channels remain in a locked state, creating an absolute refractory period during which a second action potential cannot be generated, regardless of how strong the stimulus is. After this period (during hyperpolarization), a strong stimulus can trigger another action potential; however, this is quite challenging because the membrane potential is more negative than the resting state. This refractory period is crucial for defining the minimum time interval between consecutive action potentials in a single cell, as well as for determining the typical duration of an action potential, which lasts only a few milliseconds.

A representation of a typical action potential is presented in Fig. 7, where the event is divided into five steps. First, a general stimulus alters the membrane potential, leading to various depolarizations. When these changes are not strong enough, they fail to reach the threshold; however, a sufficiently strong stimulus opens more sodium channels, generating an action potential. This is followed by the repolarization and hyperpolarization phases, ultimately returning to a resting state similar to that before the stimulus.

Once generated, the action potential travels down the axon toward the axon terminals. This movement is facilitated by the sequential opening of sodium and potassium channels along the axon. When the action potential reaches the axon terminals, it triggers the release of neurotransmitters into the synaptic cleft, where they are received by the next neuron. If these neurotransmitters result in depolarization, such as by opening sodium channels, the presynaptic neuron is referred to as an excitatory neuron, as it facilitates the generation of another action potential. Conversely, if the neurotransmitters open potassium or chloride channels, the membrane potential will undergo hyperpolarization, making the neuron less likely to trigger an action potential. In this case, the presynaptic neuron is classified as an inhibitory neuron.

Figure 7 – Schematic representation of an action potential and its phases. (1) Stimulus starts the change in the membrane potential. (2) If depolarization is passes the threshold, more sodium channels open and an action potential is generated. (3) Membrane repolarization results from closing sodium channels and opening of potassium channels. (4) Hyperpolarization due to efflux of positive ions, followed by closing of potassium channels. (5) Resting state of the membrane potential.

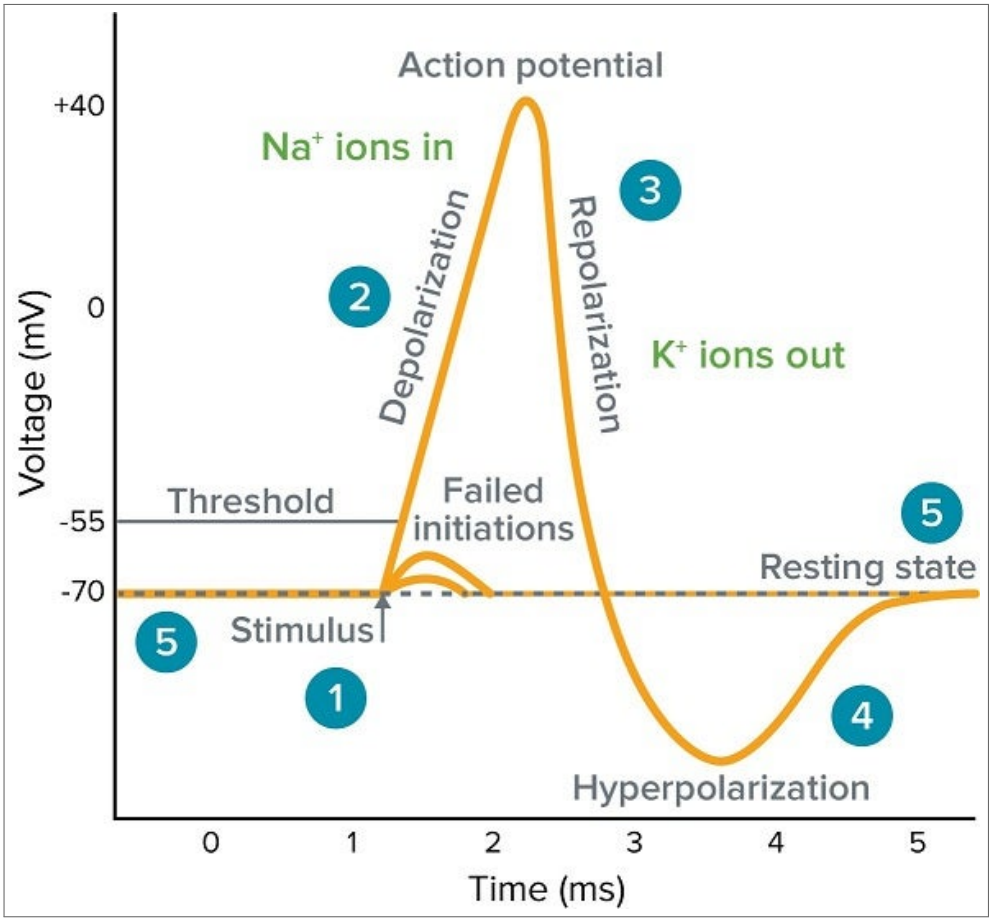

Source: from moleculardevices.com

Therefore, action potentials serve as the language of neurons, enabling them to transmit signals across vast networks and facilitating complex processes such as perception, decision-making, and movement.

The measurement of action potentials can be conducted using various methods, ranging from electric probes inserted into the intracellular medium of *in vitro* cell samples, to genetically modified neurons expressing fluorescent proteins in the cell's soma. Regardless of the method employed, action potentials consistently manifest as "all-or-nothing" events. This characteristic allows researchers to analyze them in a binary manner: either the action potential occurs, or it does not. In this context, the term "action potential" is often replaced by the term *spike*.

Neuron morphology and spike activity vary across different brain regions, each with its specific arrangement and function. In the next section, we will discuss this aspect and focus on the region studied in this work: the primary visual cortex.

2.2 THE PRIMARY VISUAL CORTEX

The central nervous system (CNS) is the body's information processing center, composed of the brain and spinal cord. The spinal cord, located within the vertebral column, consists of millions of neurons. Its primary functions are to send motor commands from the brain to the peripheral body and relay sensory information from the sensory organs to the brain. Additionally, the spinal cord performs reflex responses to specific stimuli, enabling quick actions without direct involvement from the brain. The brain is responsible for sensation, movement, emotions, communication, thought processing, memory, essential life functions, and higher-order cognitive functions. Given its numerous responsibilities, it is natural for the brain to be divided into several major regions, each with specific functions and subdivisions.

The largest region of the brain is the cerebrum, which is divided into two hemispheres: the left and the right. Although they are in constant communication with one another, the left and right hemispheres are responsible for different behaviors. The left hemisphere is more dominant in language, logic, and mathematical abilities, while the right hemisphere excels in artistic and musical situations, as well as intuition. This tendency for certain neural functions to be specialized in one hemisphere is known as brain lateralization. The outermost layer of the cerebrum, the cerebral cortex, is the primary site of neural integration in the CNS. It contains billions of neurons that execute many high-level functions of the human brain, ranging from sensory perception to abstract thinking. The cerebral cortex is the seat of our intelligence, enabling conscious thought, creativity, and voluntary actions. It is often referred to as "gray matter" because of its color, which is derived from the densely packed neurons in a tissue area that is 1 to 4 mm thick, depending on the species, and highly folded.

The cerebral cortex exhibits significant laminar differences and is organized into six distinct layers, collectively known as the neocortex or cortical layers. These layers vary in thickness, density, and cell types across different areas of the cortex, enabling each region to perform specialized functions, ranging from sensory processing to motor control and complex cognition. The outermost layer, referred to as Layer I or the molecular layer, contains very few neurons, primarily horizontal cells of Cajal. However, it is rich in dendrites and axons from neurons located in deeper layers. The molecular layer primarily serves as a communication hub, facilitating connections between cortical areas and integrating input from other layers and regions of the brain. Descending to Layer II, the external granular layer consists of small pyramidal cells and stellate cells. This layer acts as a receiving area for inputs from other cor-

tical regions and also sends outputs to these areas, making it crucial for local communication within the cortex. Layer III, known as the external pyramidal layer, contains larger pyramidal neurons compared to those in Layer II. The cells in this layer possess long axons that project to other cortical regions, both within the same hemisphere and across to the opposite hemisphere. Layer IV, called the internal granular layer, receives most of its input from the thalamus, which serves as a relay center by processing impulses from sensory receptors throughout the body and distributing the information to the appropriate cortical area. Additionally, the thalamus is responsible for regulating consciousness and sleep. For this reason, Layer IV is well-developed in regions associated with sensory perception and is composed of densely packed stellate cells, with relatively few pyramidal cells. Layer V, known as the internal pyramidal layer, consists of large pyramidal cells with branched dendrites and axons, which transmit information from this layer to other subcortical areas. Finally, Layer VI, referred to as the multiform layer, contains a mix of different cell types, including small pyramidal neurons and fusiform cells. This layer sends feedback projections to the thalamus, helping to regulate and refine the input it receives.

The cerebral cortex, sometimes referred to as the cerebral mantle, is divided into four lobes: the frontal, parietal, temporal, and occipital lobes, each with specialized functions. The frontal lobe, located at the front of the brain behind the forehead, is responsible for voluntary motor functions, reasoning, planning, problem-solving, speech, emotional expression, and serves as an inhibitory site for other brain regions. Behind the frontal lobe, near the top of the brain, is the parietal lobe, which processes sensory information such as touch, temperature, and pain, and contributes to spatial awareness. The temporal lobe, situated on the sides of the brain, is involved in hearing, memory, and language comprehension, while the occipital lobe, located at the back of the brain, is primarily responsible for processing visual information. A schematic representation of the four lobes is given in Fig. 8(a).

Within the four lobes of the brain, several regions of the cerebral cortex are localized and typically classified according to their specific functions. For instance, the temporal lobe contains various cortical areas, such as the primary auditory cortex and the olfactory cortex, which process auditory information from the ears and the sense of smell, respectively. These cortical areas are distinguished not only by their functions and anatomical locations but also by their unique cytoarchitecture. This means that the types of cells, their arrangement, and the thickness of layers vary in each area. This work utilizes recordings from the primary visual cortex, often referred to as V1, which is located in the occipital lobe and processes visual input from the retina. Therefore, a more detailed description of this area of the cortex will be

Figure 8 – The cerebral cortex and the primary viusal cortex. (a) Four lobes of the cerebral cortex, the frontal, parietal, temporal, and occipital lobes, each associated with specialized functions.(b) Illustration of the retina-thalamus pathway, where information from visual stimulus is propagated from the retina to the thalamus through the optic nerves, which cross at the optic chiasm, and continues as the optic tract. (c) The primary visual cortex (V1) is located in the occipital lobe, and consists of six layers of neurons, where a schematics of the the spatial arrangement of the main cellular is given.

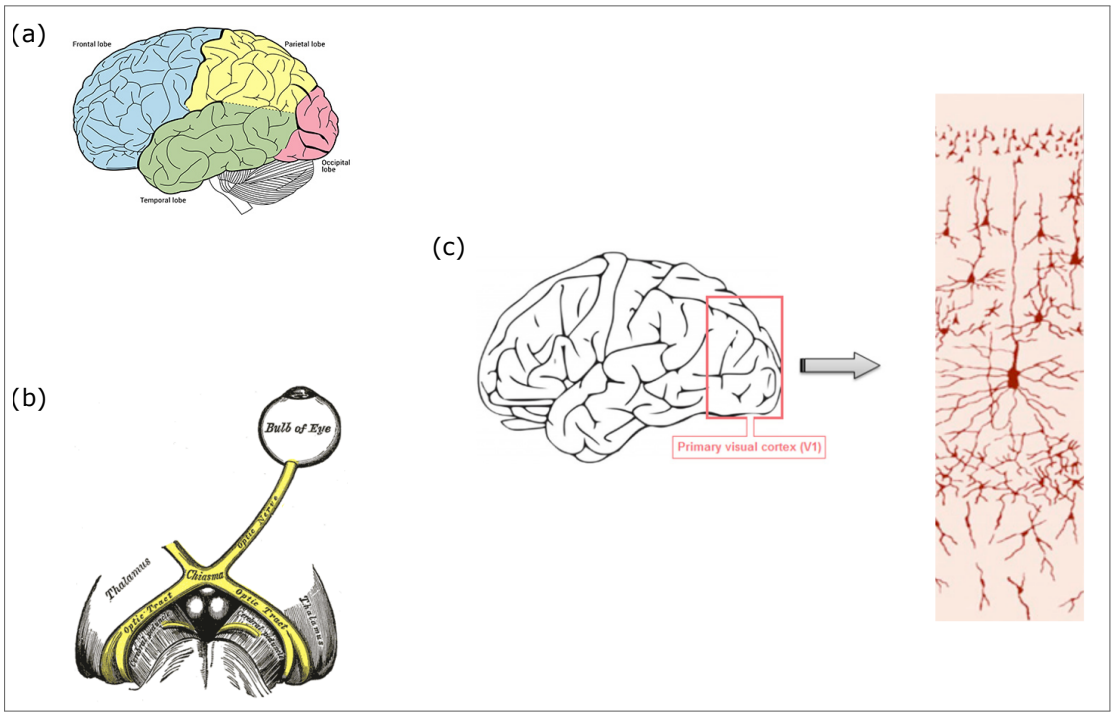

Source: adapted from SENZAI; FERNANDEZ-RUIZ; BUSáKI (2019) and Google Research

provided.

The primary visual cortex (V1), also known as Brodmann area 17 or the striate cortex, is the first cortical region responsible for processing visual information. Retinal ganglion cells receive visual data from photoreceptors in the retina and collectively transmit this information to the lateral geniculate nucleus (LGN), two small regions of the thalamus that receive input from both eyes. This transmission occurs through the optic nerve, which consists of converging axons from the retinal ganglion cells of each eye. The optic nerves cross at a point called the optic chiasm, where information from the eyes is sent to the two hemispheres of the thalamus (each hemisphere contains one LGN) through the continuation of the optic nerve after crossing, known as the optic tract (see Fig. 8(b)). After processing the visual signals, the LGN sends the integrated information to the primary visual cortex (V1) via a direct pathway of axons called the optic radiation. This information primarily targets layer IV of V1, which is critical for sensory input and is further divided into sublayers (IVa, IVb, IVc), each responsible for processing different aspects of visual stimuli, such as light intensity and orientation. A schematic representation of the localization of V1 and it's layers is provided in Fig. 8(c).

Layers II and III of the primary visual cortex (V1) are involved in integrating visual information and transmitting processed signals to higher visual areas, specifically projecting to regions such as V2, V3, V4, and the middle temporal area (MT or V5). These areas further process the information to handle more complex visual tasks, such as object recognition (managed by V4) and motion detection (managed by MT/V5). Additionally, layers II and III contribute to feedback loops with regions in the parietal and temporal lobes, integrating visual input with spatial orientation, attention, and memory functions. Layers V and VI project to subcortical structures, playing roles in modulating signals that return to the thalamus. This layered architecture enables the primary visual cortex to analyze and interpret basic visual features such as contrast, edges, and motion, forming the foundation for more complex visual perception.

2.3 LOCAL FIELD POTENTIAL

2.3.1 Extracellular potentials

Electric current contributions from all active cellular processes within a volume of brain tissue superimpose at a given location in the extracellular medium and generate a scalar potential, V_e. A difference of this potential between two locations give rise to electric fields that can be monitored by placing extracellular electrodes with high time resolution and can be used to interpret many facets of neuronal communication and computation. Traditionally, V_e has been referred to as different names depending of the spatial and temporal aspects of the recording method. For instance, electroencephalography (EEG) is one of the oldest and most widely used method for the investigation of the electric activity of the brain. EEG is a non-invasive method that involves placing electrodes on the scalp to record electrical activity, integrating over $10cm^2$ of area. While it is very noisy and has lower spatial resolution compared to intracranial methods, it is widely used in both clinical and research settings.

Electrocorticography (ECoG) uses subdural platinum–iridium or stainless steel electrodes to record electric activity directly from the surface of the cerebral cortex, thereby bypassing the signal-distorting skull and intermediate tissue, making it much less noisy compared to EEG. The spatial resolution of the recorded electric field is less than $5mm^2$. Magnetoencephalography (MEG): uses superconducting quantum interference devices (SQUIDs) to measure tiny magnetic fields outside the skull generated from neuron currents. MEG is non-invasive and has a relatively high spatial-temporal resolution (1 ms, and 2–3 mm in principle), and because of

that, has become a popular method for monitoring neuronal activity in the human brain.

While EEG, MEG, and ECoG primarily sample electrical activity occurring in the superficial layers of the cortex, electrical events in deeper layers can be recorded by inserting metal or glass electrodes or silicon probes with very high sampling rates (10–40 kHz) into the brain. This type of recording is known as the local field potential (LFP), which represents the summed electrical activity of a population of neurons, primarily reflecting synaptic activity, including excitatory and inhibitory postsynaptic potentials. Unlike action potentials, which are discrete spikes of electrical activity generated by individual neurons, LFPs provide a more holistic view of the brain's electrical dynamics.

2.3.2 LFP sources

LFPs are generated by the flow of ionic currents through the extracellular space surrounding neurons. These currents are predominantly driven by synaptic activity, creating electric dipoles as ions enter and exit the neurons. The primary sources of LFPs are synaptic activities, specifically the excitatory and inhibitory postsynaptic currents. Fig. 9 illustrates how these synaptic activities affect the LFP. In Fig. 9(a) we see a simulation of the LFP traces (gray waveforms) in response to an excitatory synaptic current injected into the distal dendrites of a pyramidal neuron. Since excitatory currents induce an influx of positive ions into the neuron, the LFP traces near the injection site (blue circle) show amplitude depressions (negative values), with this region (indicated by blue dashed lines) being referred to as *sinks*. To achieve electroneutrality, the extracellular sink needs to be balanced by an extracellular *source* (red lines), which represents an opposing ionic flux from the intracellular to the extracellular space, known as *return current*, flowing along the neuron. These sources (positive waveforms) can be observed near the mid-dendrite (green triangle) and the soma (orange square) of the cell. The power spectra of the membrane potential in these regions are also shown, with higher frequencies being more prominent in the sinks. Inhibition synaptic currents can also significantly affect the LFP, as illustrated in Figs. 9(b) and (c). In both cases, the spiking activity of inhibitory neurons connected to a postsynaptic neuron induces a hyperpolarization effect on the target cell's membrane potential. More specifically, in Fig. 9(c) we see LFP recordings at six sites (blue squares) generated by an induced action potential of an inhibitory basket neuron forming a synapse with a pyramidal neuron in the hippocampus. It can be observed that the hyperpolarizing currents generate a large positive response near the soma of the target cell.

In Fig. 9(d) we see an illustration of a spike's extracellular contribution to the LFP in the vicinity of the spiking pyramidal cell. The magnitude of the spike is normalized, with the peak-to-peak voltage range indicated by the color of the traces. Unlike synaptic currents, the amplitude of the spike-induced LFP decreases rapidly with distance from the soma, without a change in polarity within the pyramidal layer, as illustrated in the highlighted box. With voltage in scale, the distance dependence of the LFP amplitude within the pyramidal layer (bottom left panel) demonstrates that the contribution of a single spike diminishes to nearly null within a few hundred micrometers from the soma. Since spikes are very rapid events, the contribution of a single action potential to the LFP is minimal. However, synchronous spikes from many neurons can significantly contribute to the high-frequency components of the LFP. In fact, one of the goals of this work was to explore the relationships between LFP recordings and the temporal structures of spiking neuronal populations.

Although synaptic currents are the primary source of the LFP, followed by the synchronization of neuron populations' spikes, there are many other contributors to the LFP. These include long-lasting (10–100 ms) calcium-mediated spikes, neuron-glia interactions, ephaptic effects, neuronal geometry, network architecture, and others. As a result, the LFP is a complex signal composed of a wide range of temporal properties. Extracting micro-level information solely from LFP recordings is a challenging task. With this in mind, researchers have been analyzing LFPs from various perspectives.

2.3.3 LFP Frequency Bands

The LFP can be analyzed under different domains, depending on the type of meaningful information one wish to extract from the recorded signal. For instance, the time-domain analysis involves analyzing the raw signal over a period of time, looking for, either event-Related Potentials (EPRs) or Inter-peak latencies (IPRs), that correspond to specific stimuli or behaviors.

Since LFP signals are typically tracked over a relatively large pass-band, ranging from 0 to 250 Hz, they are predominantly studied using frequency-domain analysis. This set of techniques involves performing Fourier transforms and other spectral analyses to decompose the LFP into different frequency bands, each associated with specific types of neuronal activity and cognitive functions. Given that the LFP primarily reflects the summed synaptic activity of a brain tissue region, this type of analysis is crucial for identifying dominant brain rhythms

Figure 9 – Examples of excitatory and inhibitory postsynaptics currents as contributions to the LFP.(a) Simulation of the LFP traces (grey) in response to an excitatory synaptic current (illustrated in the box) injected into the distal dendrite of a cortical neuron. Red and blue lines correspond to positive and negative values for the LFP, respectively. The power spectra of the membrane potential is also shown, for the injection site (blue circle), mid-dendrite (green triangle), and soma (orange square). Note that high frequency effects decreases with the distance from the synaptic site.(b) Inhibitory connection between interneurons presented with a cross-correlogram between the spikes of the reference neuron (red line) and the other cell, and, superimposed on it, the average of the membrane potential of the affected cell (blue). Note the hyperpolarizing effect of the inhibition corresponding to a decreased spike discharge.(c) Inhibition-induced LFPs were generated near a pyramidal neuron (bottom cell) by intracellularly induced action potentials in a nearby basket cell (top cell), and were recorded at six sites in multiple regions of the hippocampus. The mean LFP amplitude at each site is shown by the blue squares and examples of LFP traces (blue) from the sites and the action potential of the basket cell (red trace) are shown on the right. Note that the largest positive response by inhibition-induced hyperpolarization occurs near the soma. SLM, stratum lacunosum moleculare; SO, stratum oriens; SP, stratum pyramidale; SR, stratum radiatum.(d) Extracellular contribution of a spike to the LFP in the vicinity of the spiking pyramidal cell, with the magnitude of the spike normalized. The peak-to-peak voltage range is indicated by the colour of the traces. Note that the spike amplitude decreases rapidly with distance from the soma, without a change in polarity within the pyramidal layer (the approximate area of which is shown by the box), in contrast to the reversed polarity signals both above and below the pyramidal layers formed along the vertical axis. The distance-dependence of the spike amplitude within the pyramidal layer is shown (bottom left panel) with voltages drawn to scale. The same traces are shown normalized to the negative peak (bottom right panel), showing widening of the spike with distance from the soma.

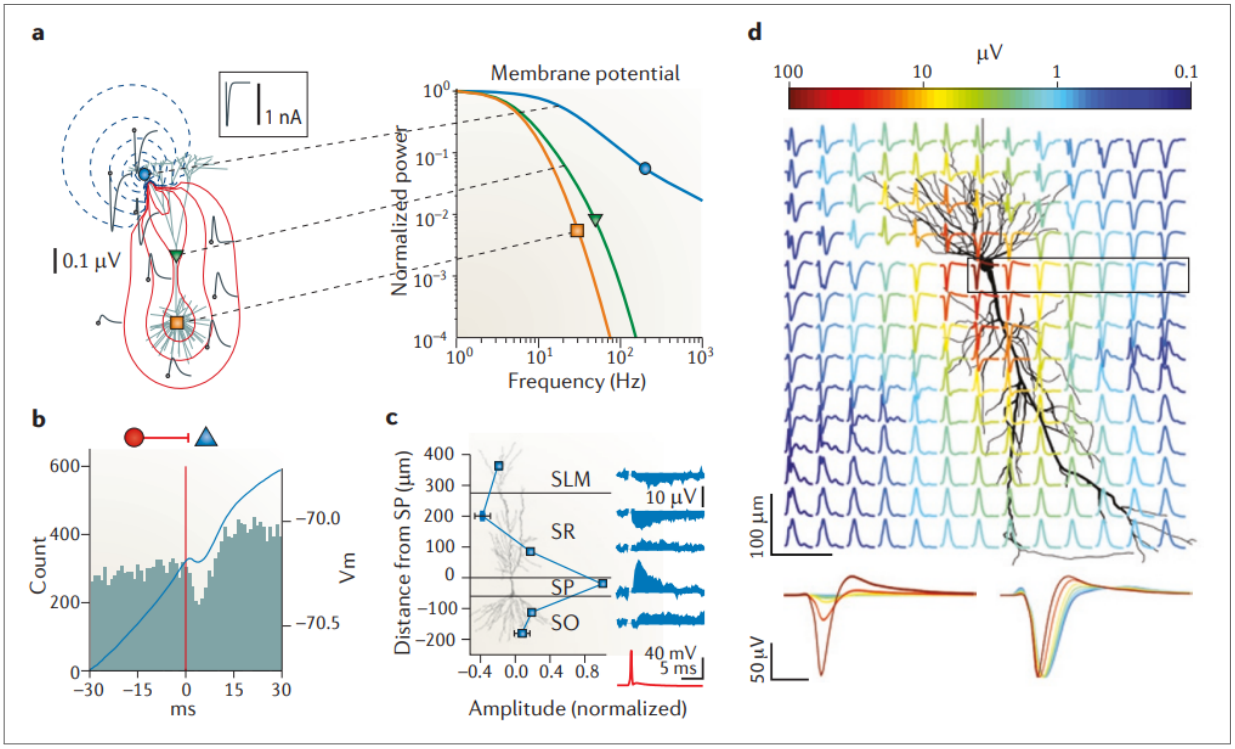

Source: from BUZSÁKI; ANASTASSIOU; KOCH (2012)

and their temporal changes. In fact, measures of coherence and connectivity between brain regions are often calculated within the context of the spectral composition of the LFP. There are even discussions suggesting that the spectral composition of the LFP plays a significant role in its spatial reach, with slower frequency bands affecting more distant regions compared

to faster bands (KAJIKAWA; SCHROEDER, 2011; LINDÉN et al., 2011).

The frequency bands themselves are associated with various neural processes and cognitive states, and they have historically been named after Greek letters. The delta band (1-4 Hz) is often linked to deep sleep stages, particularly non-rapid eye movement (NREM) stages 3 and 4, commonly referred to as slow-wave sleep (SWS). The theta band (4-7 Hz) tends to peak during states of drowsiness or meditation; however, in the hippocampus, this frequency band is also associated with memory encoding, retrieval, and navigation. The alpha band (7-12 Hz) is commonly observed during relaxed alertness and peaks when the eyes are closed during quiet wakeful states. Although it was the first brain rhythm discovered in 1924 by Hans Berger with the invention of EEG, debates continue regarding the origin and functions of the alpha band. Recent research suggests that alpha rhythms play a role in inhibiting irrelevant stimuli and coordinating networks (KLIMESCH, 2012). As frequencies increase, the bands widen their ranges, leading to the coexistence of several rhythms, some of which are excitatory while others are inhibitory. The beta band (12-30 Hz) is associated with focused mental tasks such as problem-solving, decision-making, and higher states of alertness. It is also prominent in motor control, particularly during movement planning. Elevated beta activity can be linked to states of anxiety or tension, with higher levels indicating increased arousal or stress responses. The gamma band (30-70 Hz) is associated with enhanced sensory processing and attentional mechanisms, especially in the visual and auditory domains. This band is also involved in learning, memory, and precise, complex motor control. Some discussions suggest that gamma oscillations relate to states of conscious awareness by integrating disparate pieces of information into a coherent perceptual experience (SUMMERFIELD; JACK; BURGESS, 2002). However, the mechanisms by which gamma activity generates different states of consciousness remain unknown. Thus far, the characteristics of each band described are what one would expect from a healthy brain. However, as will be discussed later, unnatural levels of specific bands can be associated with a wide array of disorders. An illustration of a 10-second LFP signal recording filtered by each described band is shown in Fig. 10.

To quantify the presence of frequency bands in LFP signals, it is common to calculate the power spectrum density (PSD) of the signal. The PSD describes graphically how the power of the signals is distributed along the frequencies, proving to be an excellent tool in identifying peaks of frequency bands. The PSD of LFPs presents a scaling behavior of the type $1/f^{\alpha}$, where α achieves values, typically, around 1. This $1/f$ aspect suggests that the underlying process have a scale-invariant nature, which means they exhibit similar patterns

Figure 10 – Local field potential (LFP) filtering process is illustrated as a representative 10-s signal in resting state with synchronously recorded spike raster and an LFP spectrogram. Each band is represented by a Greek letter and are associated with specific cognitive functions. The Delta band (1-4 Hz) is linked with deep sleep stages, theta band (4-7 Hz) is usually associated with memory and navigation, Alpha band (7-12 Hz) is observed in relaxed awake states, Beta band (12-30 Hz) is associated with motor control and alertness wake state, and the gamma band (30-70 Hz) is often associated with higher-order cognitive functions.

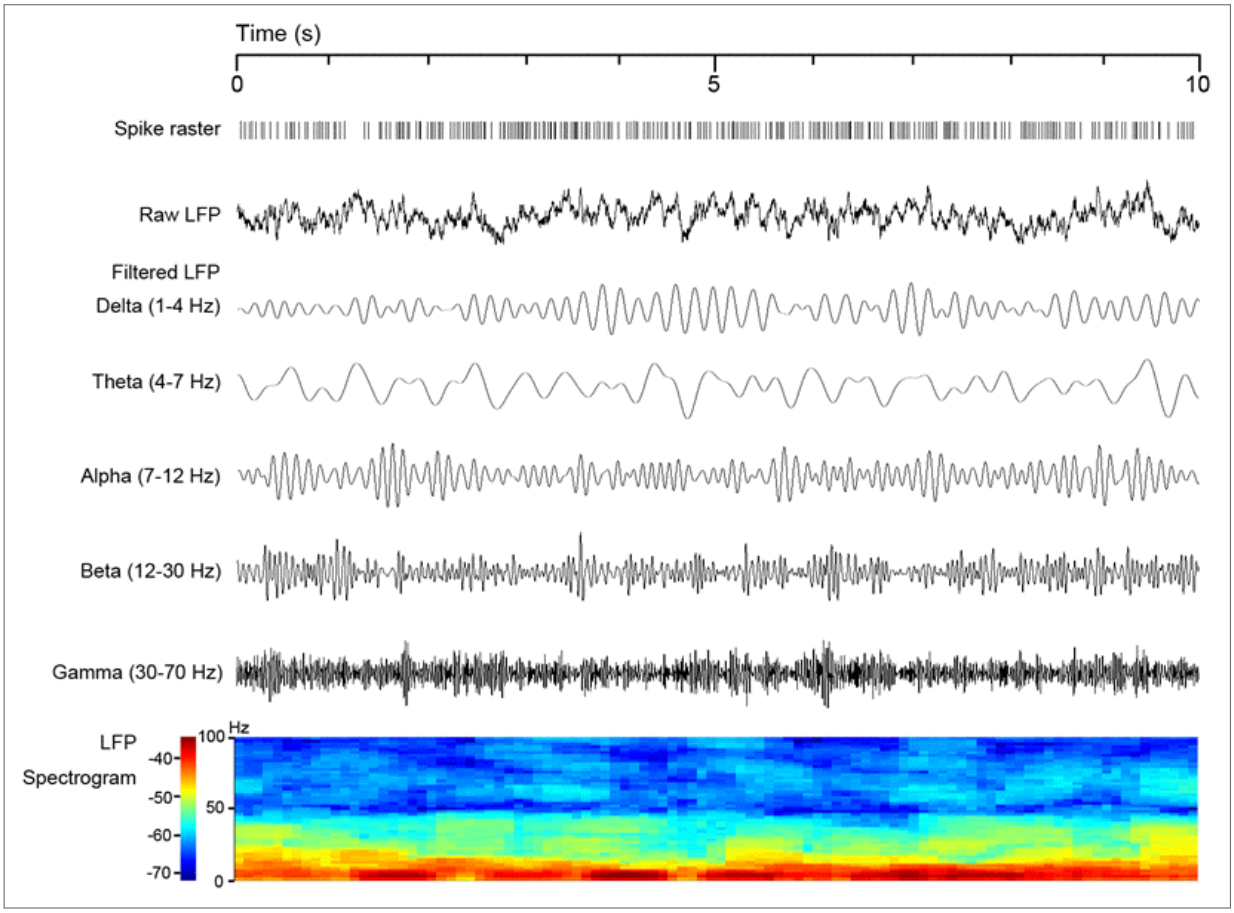

Source: from ZHANG et al. (2021)

across different temporal scales.

2.3.4 LFP applications

Local field potentials (LFPs) are ideal for investigating the coordinated activity of neural circuits and understanding how different brain regions collaborate during tasks such as sensory processing, motor control, and cognitive functions. LFP recordings are commonly used in both animal models and human studies, including patients with epilepsy or Parkinson's disease, where they assist in identifying abnormal neural rhythms associated with these pathological conditions.

In addition to their role in basic neuroscience, LFPs have various practical applications,

particularly in brain-machine interfaces (BMIs) and neuroprosthetics. Because LFP signals are generally more stable over time compared to single-neuron recordings, they provide a reliable source of information for decoding motor intentions or cognitive states. For instance, in BMIs, LFPs are used to translate brain activity into commands that control prosthetic limbs, enabling individuals with paralysis to regain motor function.

Clinically, local field potentials (LFPs) have significant applications in diagnosing and treating neurological disorders. One of their primary uses is in guiding deep brain stimulation (DBS) therapy for conditions such as Parkinson's disease, essential tremor, and dystonia. By recording LFPs from implanted electrodes, clinicians can monitor the abnormal neural activity associated with these disorders and adjust DBS settings to more precisely target pathological brain rhythms, thereby improving symptom management. LFPs are also utilized in epilepsy treatment, where they aid in identifying seizure foci during surgical planning. By analyzing abnormal electrical patterns, clinicians can localize and resect the brain areas responsible for generating seizures.

2.4 SURGERY RECORDING

Both local field potentials (LFPs) and action potentials of neurons can be extracted from living animals using different methods. In this work, we utilized electrophysiological recordings obtained from rats and mice by inserting multi-electrode silicon probes with high recording rates into the primary visual cortex (V1) of each animal. This procedure involved performing a craniotomy, which is the surgical removal of a portion of the skull to expose the brain cortex, followed by the careful insertion of the probes into the region of interest to record the electrical activity of that tissue. A basic representation of an electrophysyology recording of a rodent is given in Fig. 11(c), where recorded signals are converted, amplified and digitized at very high sample rates. The result signal is then processed and analyzed with the use of computer software.

2.4.1 Anesthetized rats

The *in vivo* experiments targeted recordings in albino urethane-anesthetized rats ($n = 4$, Wistar Han, male, 350-500 g, 3-6 months old, 1.44 g/kg urethane), from the primary visual cortex (V1, Bregma: AP = -7.2 mm, ML = 3.5 mm). The use of the urethane anesthetics is

not by chance, as it has the characteristics of accessing many spontaneous activity patterns, which is desired for the goal of this work, since it requires access to a continuum of cortical states.

Such as is illustrated in Fig. 11(a), data has been recorded by using a 64-channel silicon probe, with six shanks, 200 μm apart, inserted around the central coordinate, along the direction defined by the anterior-posterior axis (PAXINOS; WATSON, 2016). Each shank in this probe contains 10 channels, separated by 20 μm, accessing deep layers of the cortex. The extra-cellular signal in each channel was sampled at 30 kHz (Intan RHD2164, 16 bits/sample), based on Open Ephys acquisition system (SIEGLE et al., 2017). The *in vivo* experimental procedures, encompassing animal housing, surgical interventions, and data recordings, strictly adhered to the FELASA guidelines (NICKLAS et al., 2002) and were conducted in full compliance with European Regulations (European Union Directive 2010/63/EU). Both the animal facilities and the personnel responsible for conducting these experiments were officially certified by the Portuguese regulatory body, DGAV (Direção-Geral de Alimentação e Veterinária). Furthermore, all research protocols underwent thorough scrutiny and received approval from the Ethics Committee of the Life and Health Sciences Research Institute (ICVS). More detailed information can be found in the recent studies (VASCONCELOS et al., 2017; FONTENELE et al., 2019). Additionally, we employed non-albino urethane-anesthetized Long-Evans male rats ($n = 3$, 350–500 g, 3–6 months old, 1.44 g/kg urethane), under approval by the Federal University of Pernambuco (UFPE) Committee for Ethics in Animal Experimentation (23076.030111/2013-95, 12/2015, and 20/2020).

2.4.2 Freely moving mice

We also used recordings from 19 freely moving mice, implanted with 64-site linear silicon probe (H3, Cambridge NeuroTech). This probe is represented in Fig. 11(b) and, although it captures a smaller neuron population when compared to multi-shank probes, it's ideal for studying the laminar structure of the cortex, recording activity from neurons along all cortex layers. The freely moving mice database is public from Buzsáki's lab, as recently published (SENZAI; FERNANDEZ-RUIZ; BUSáKI, 2019). In summary, surgery and electrode implantation, extracellular electrophysiological recording, electrolytic lesions, histological processing, spike sorting, and detection of monosynaptic functional connectivities were performed. Electrophysiological data were acquired using an Intan RHD2000 system, digitized with a 20 kHz rate, and the

Figure 11 – Schematics representations of silicon probes used in the experiments and basic recording setup. (a) Buzsaki64sp silicon probes are 64-channel probes with six shanks, 200 μm apart, which are suited for recording distant neuron populations at deep layers of the cortex. (b) NeuroTech H3 is a vertical 64-channel silicon probe ideal for studying the laminar structure of the cortex, recording activity from neurons along all cortex layers. (c) A basic representation of an electrophysiology recording, the probes are inserted in the animal cortex and connected to computers through wires. The signal from the electrodes are amplified and digitized at high sample rates, and are ultimately analyzed by using tracking software.

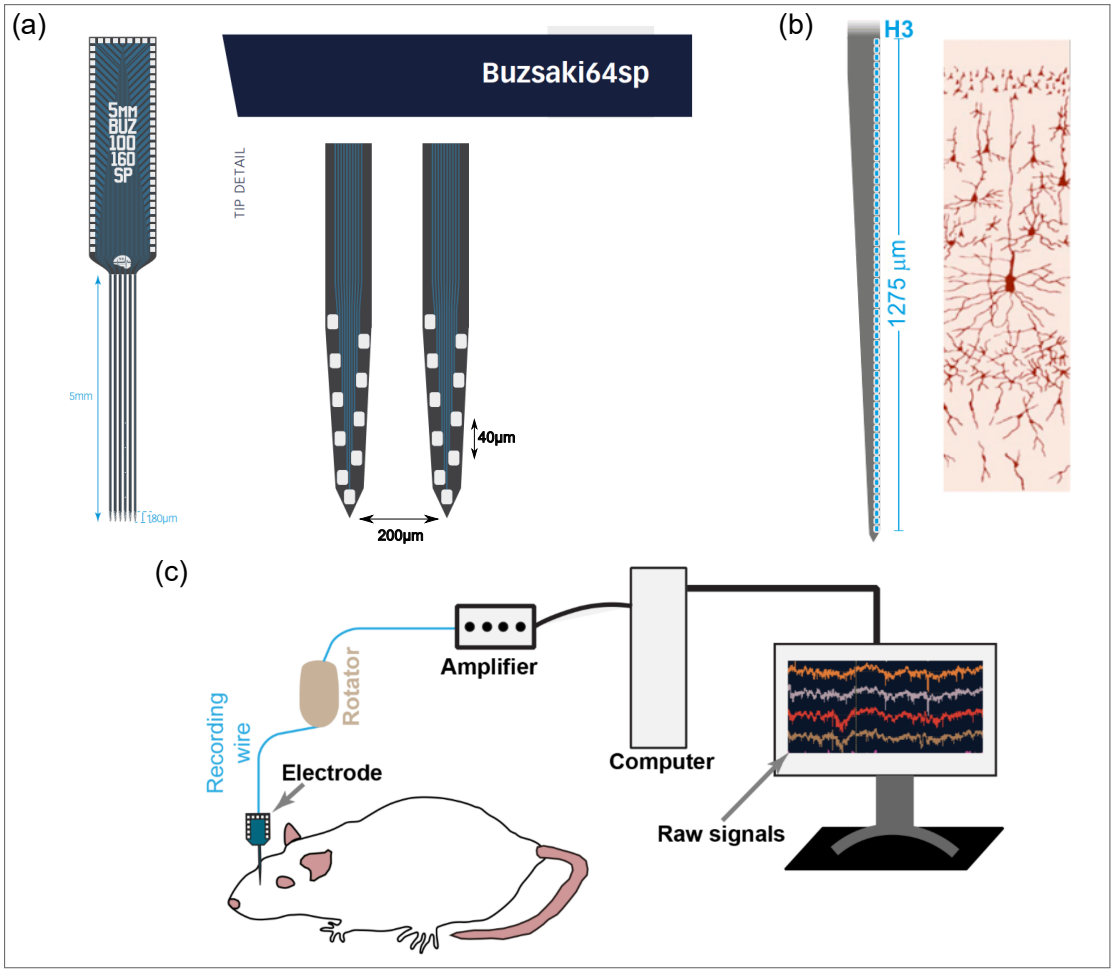

Source: adapted from SENZAI; FERNANDEZ-RUIZ; BUSáKI (2019) , neuronexus.com, and Google Research

wide-band signal was downsampled to 1.25 kHz for use as the LFP signal.

Since the mice were freely moving, the detection of spikes was much more frequent due to the absence of inhibitory effects from anesthesia. Additionally, freely moving animals can access different behavioral states; for instance, the mice could be awake or in various stages of sleep, which were accurately tracked. These behavioral states were utilized in this work, as we analyzed the statistical properties of the local field potentials (LFPs) across them. Furthermore, the laminar structure of the silicon probe facilitated our research into the interactions among cortical layers in the primary visual cortex.

2.5 DATA ANALYSIS

Since the raw data recorded from the experimental setups described in the previous section covers a wide range of frequency bands (up to 20-30 kHz), we can obtain different datasets depending on the timescale of interest by using various data analysis techniques. In the case of the local field potential (LFP), we can easily extract it from the raw data by applying frequency filters and tracking it at a desired sampling rate. In the context of this work, the LFP from all animals was extracted using a low-pass Butterworth filter with a cutoff frequency of 200 Hz, and it was tracked with a sample rate of 500 Hz. A Butterworth filter, named after Stephen Butterworth (BUTTERWORTH, 1930), is designed to have a flat frequency response in its pass-band, meaning it causes no ripples and smoothly attenuates frequencies beyond the cutoff.

With regard to spiking activity from neuron populations, further techniques are necessary to identify the moments where action potentials were triggered, and, furthermore, associate individual neurons to specific spikes. These techniques are usually grouped together in a process named *spike sorting*.

2.5.1 Spike Sorting

Spike sorting is a class of computational techniques used in neuroscience to isolate and classify action potentials, commonly referred to as spikes, recorded from various regions of the brain, such as the cortex. In simpler terms, spike sorting involves organizing these spikes, which is especially important when multiple neurons are being monitored simultaneously using extracellular electrodes. This process is crucial for understanding the activity of individual neurons within a population, as it allows researchers to find correlations between the spiking patterns of different neurons.

The first key step in spike sorting is filtering the raw data within a frequency range associated with action potentials. Typically, a band-pass filter is applied to isolate the frequencies where spikes are most likely to occur, generally between 300 Hz and 3 kHz. This filtering process removes slower sources, such as synaptic currents and other contributors to the local field potential (LFP), as well as drift and low- and high-frequency noise. The next step involves applying spike detection algorithms to identify spikes from the filtered extracellular potential. This process includes marking the time points where the filtered potential exceeds a defined

threshold, which is typically based on the amplitude of the signal's statistical elements. This threshold is commonly expressed as a multiple of the standard deviation of the signal's noise, serving to effectively separate spikes from noise.

Once the spikes are accurately time-marked, a time window is selected around each spike event to capture the full shape of the spike waveform. This process, known as windowing, requires the window to be large enough to encompass the entire spike, including its ascending and descending phases. Following this step, the waveforms are aligned using a reference point, typically the peak amplitude of the spike. The steps described so far—filtering the raw data, detecting the spikes, and aligning the spikes—are illustrated in Fig. 12.

Figure 12 – Illustration of the first steps in the spike sorting process. First, the raw data is processed using band-pass filters, then a threshold for detecting spikes is defined, and lastly, spikes waveforms are aligned using a reference point.

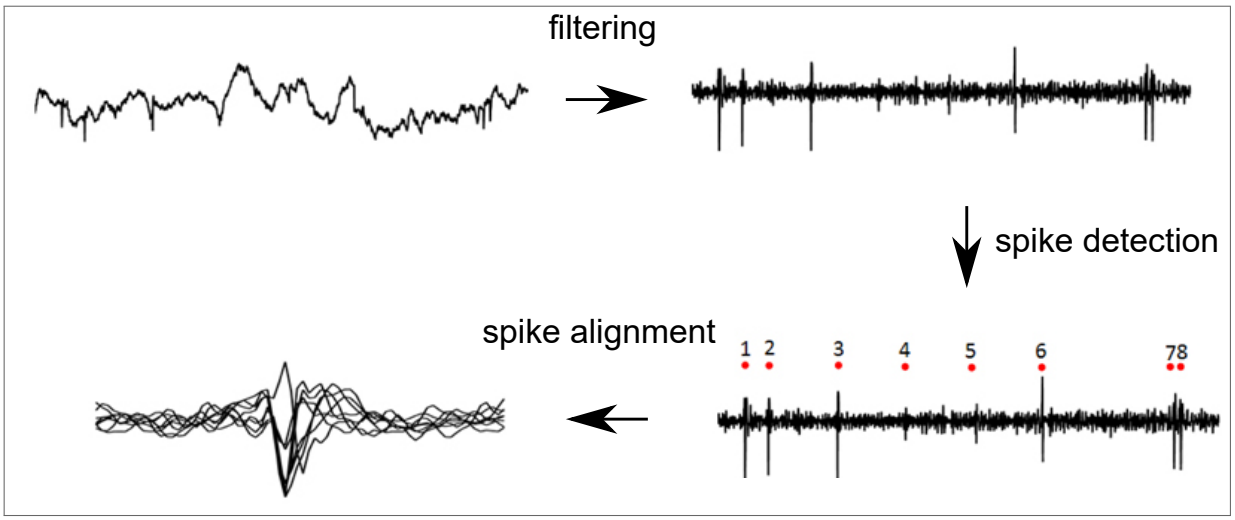

Source: adapted from PETRANTONAKIS; POIRAZI (2015)

The next steps in the spike sorting process focus on assigning each spike waveform to a specific neuron. Just as each person's voice has unique vocal features, each neuron produces distinct waveforms, allowing for the extraction of features to categorize the spikes. A common method for feature extraction is Principal Component Analysis (PCA), which reduces the dimensionality of the waveforms by projecting them into their principal components—a set of orthogonal vectors that capture the most variance in the data. Typically, the first two principal components are used to plot the data in two dimensions, facilitating the visual identification of clusters of closely related data points. Once the spike waveforms are represented by a set of principal components, clustering algorithms are applied to group spikes that share similar features into clusters, with each cluster corresponding to a different neuron. The choice of clustering method depends on the specific situation. For instance, if the number of clusters

is known beforehand, K-Means clustering is a simple and effective algorithm that groups data points into k clusters based on their distance to the cluster centroids. Conversely, if the number of clusters is unknown and they are non-spherical or vary in size, density-based clustering algorithms are preferred. Finally, a manual curation step is often necessary to review and adjust the automatic clustering. This involves inspecting the now-sorted waveforms to ensure that the sorting is biologically plausible. Fig. 13 illustrates the schematic steps of a typical spike sorting process using PCA, from spike extraction from the dataset to the sorting of spike waveforms from different neurons.

Figure 13 – Schematics of a spike sorting process using principal components analysis (PCA). The spikes are extracted from the datasets and are presented as aligned waveforms, Then, PCA is applied to extract features from each waveform. Clustering methods are used to group spikes that share similar features and assign each detected spike to the neuron that generated it. Finally, biological validation of the process can be done by sorting the waveforms.

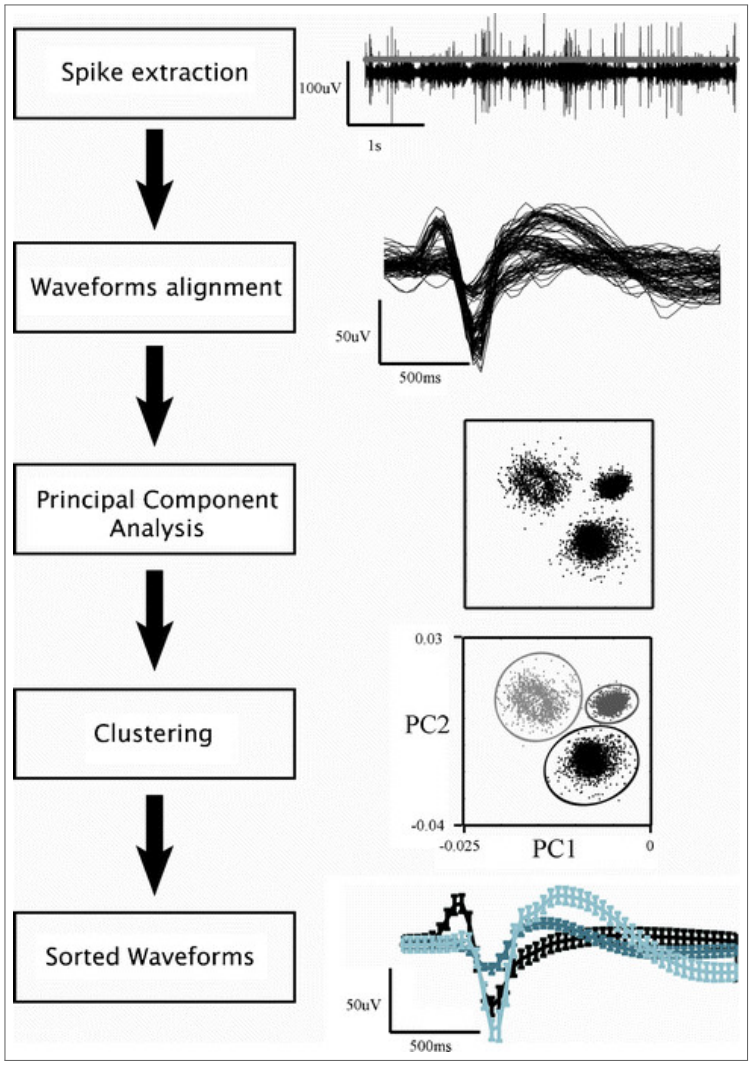

Source: from VYAZOVSKIY; OLCESE; TONONI (2011)

By identifying spikes generated by individual neurons, spike sorting facilitates the study of

single-unit activity (SUA). However, there are cases where spike sorting cannot clearly separate individual neurons. In these instances, the sorted waveforms represent the combined activity of multiple neurons, known as multi-unit activity (MUA). Although less precise than SUA, MUAs are still valuable for studying the dynamics of neuron populations. In the datasets used in this work, SUA and MUA encompassed a total of 2,535 neurons: 833 from albino rats, 921 from non-albino rats, and 781 from freely moving mice. The average number of neurons per recording for SUA and MUA was, respectively, as follows: 75 ± 15 and 132 ± 15 for albino rats, 89 ± 23 and 241 ± 79 for non-albino rats, 78 ± 22 and 33 ± 12 for freely moving mice.

With the spike times and neurons list in hand, we can treat the spikes as "all or nothing" events in order to model a basic neuronal spiking data as a set of *spike trains*, where each spike train can be defined as

$$s_k(t) = \sum_{t_i \in T_k} \delta(t - t_i), \tag{2.2}$$

where T_k is a list with the spike times of the k-th neuron within the neuronal population. Eq. 2.2 implies that, when modelled as a spike train, the only information necessary to define a spike is the spike time and the neuron that generated it, disregarding the shape of the waveform, hence the "all or nothing" expression. Based on Eq. 2.2, we can define a *instantaneous firing rate* for each neuron as

$$r_k(t, \Delta t) = \frac{1}{\Delta t} \int_t^{t+\Delta t} s_k(\tau) d\tau, \tag{2.3}$$

where Δt defines the time resolution of this measure, commonly known as *bin* in the jargon. Once one selects the bin size, typically from 10-50 ms, the results from Eq. 2.3 is discrete and can be represented by a corresponding time series, $r_{k,i}$, with i representing each bin window. The population firing rate can be simply calculated by $r_i = \sum_k r_{k,i}$.

Spike trains are graphically represented as raster plots, with the y-axis representing all the SUA or MUA, with filled points representing triggered spikes. These raster plots are usually accompanied by the firing rate as a function of time, as is illustrated in Fig. 14.

Observing the raster plot in Fig. 14, one might notice the synchronized bursts of spikes followed by desynchronized activity. These bursts are not necessarily caused by external stimuli affecting the population of neurons, in fact, they can arise from the spontaneous activity of the neuron population, reflecting a specific *cortical state* that generate this spiking pattern.

Figure 14 – Illustrative raster plot (top) and firing rate (down) of a population of neurons as a function of time. Each filled point in the raster plot represent a spike of a specific neuron at a specific time, and the firing rate is expressed as a summed activity of all neurons.

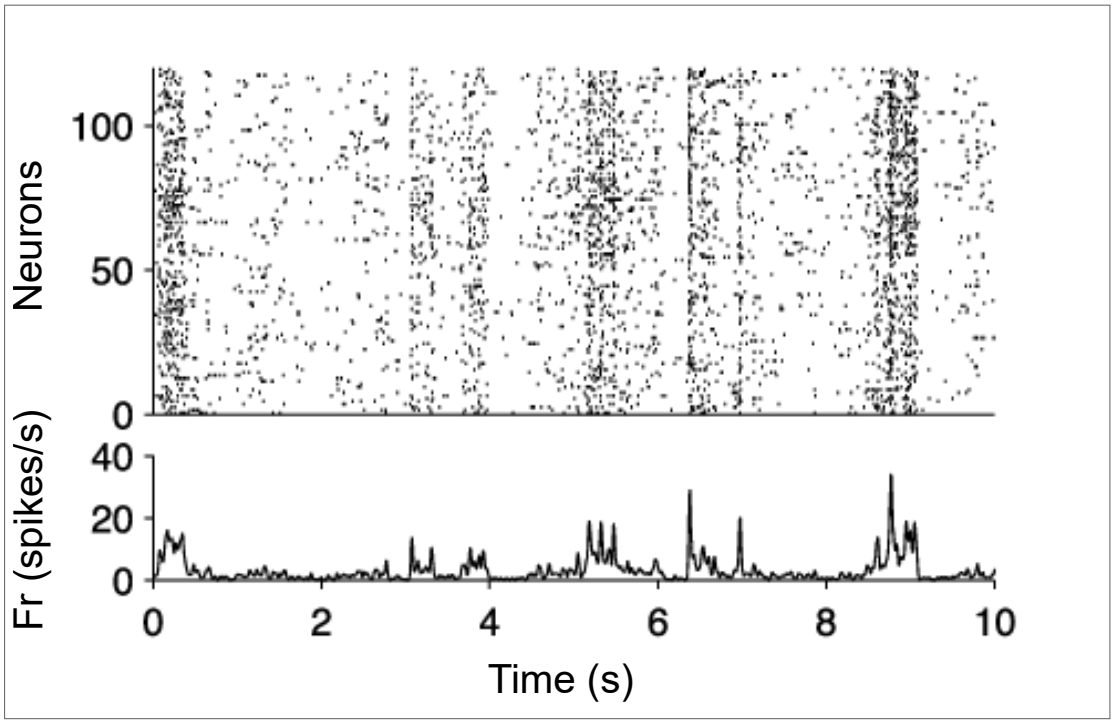

Source: adapted from KASS; KELLY; LOH (2011)

2.5.2 Cortical States and the Coefficient of Variation

Cortical activity in sensory areas is not solely dictated by sensory inputs; it reflects an interaction between external stimuli and spontaneous activity. The characteristics of these spontaneous patterns and their interaction with external stimuli are influenced by cortical states, which can be defined using various measures. Initially, cortical states were identified as patterns in EEG data. However, they can also be defined based on the spiking patterns of neuronal populations, the spectral decomposition of local field potentials (LFPs), neuronal correlations, and even intracellular potentials.

In Fig. 15, we see an illustration of two different cortical states seen in awake rodents, which can be characterized by using different neural signals: small spiking population (coloured raster plots), intracellular membrane potential (red trace), and cortical LFP from deep layers (gray trace). In Fig. 15 (a) the rodent is in a drowsy or dormant state, which, in terms of cortical activity, is usually associated with a more synchronized state. Here, the spiking activity of neurons is highly positively correlated, resulting in coordinated periods of global firing and silence, as shown in the spike raster plot. These periods of absence of spikes, commonly

Figure 15 – Illustration of two extremes cortical states seen in awake rodents. (a) In synchronized states, neurons in a populations shows propensity to fire when in a up phase, and present reduced or absent spiking in down phases (coloured raster plots). In intracellular potentials (red trace), these phases are followed by their respective depolarization and hyperpolarization effects. The LFP in this state (gray trace) has strong presence of slow waves. This type of activity is seen in drowsy animals. (b) In desynchronized states, the coordinated silences in the spiking activity are absent, losing a global idea of up and down phases. In this case, slow fluctuations in the intracellular potential and the LFP are suppressed. This type of activity is typical of alert animals.

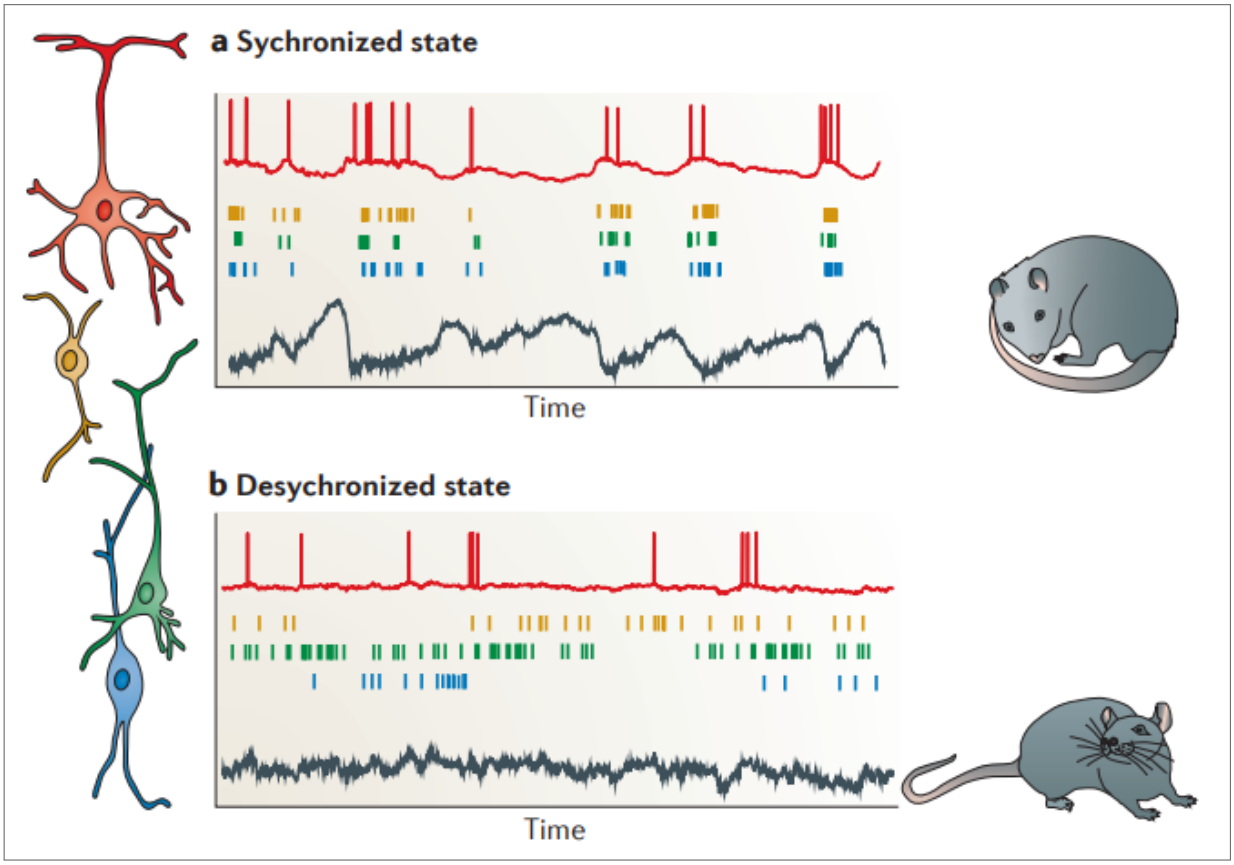

Source: from HARRIS; THIELE (2011)

referred to as down phases, can be observed in the intracellular potential as long depolarizing and hyperpolarizing effects. Conversely, the firing periods (up phases) appear as rapid peaks in the membrane potential. The LFP during this state exhibits high-frequency activity in the up phases and slow, smooth waves in the down phases. In the desynchronized state, seen in Fig. 15 (b), the coordinated silences in spiking activity are absent, disrupting the concept of global up and down phases. In this scenario, the pairwise spike correlations within the population are close to zero, indicating that neurons fire independently of one another. Additionally, slow waves in both the intracellular potential and the LFP are suppressed in this state, which is typically associated with alert animals.

These two different states depicted in Fig. 15 represent extremes of a continuum, with various cortical states existing between them. So, in order to correctly investigate how cortical

activity changes along cortical states, we need a measure to quantify such states. In this work, we will measure the cortical states by using spiking activity of neuronal populations over long periods of time, in particular, we will take time series of the instantaneous firing rate of a group of neurons, defined in Eq. 2.3, and divide it in 10 seconds long time windows. Then, for each time window, we will calculate the coefficient of variation, abbreviated by CV, defined as

$$CV_i = \frac{\sigma_i}{\mu_i}, \tag{2.4}$$

where σ_i and μ_i are, respectively, the standard deviation and average of the population firing rate r_i of each time window i. The interpretation of CV is quite direct, if σ_i is small compared to μ_i, yielding a small CV, coordinated silences is reduced in that time period, which would associate this window with a highly desynchronized state. If, on the other hand, σ_i is larger than μ_i, yielding a CV higher than 1, coordinated silences are strongly present, which would associate the window with a more synchronized state.

The minimum and maximum values of the coefficient of variation (CV) depend on various factors, including animal species, cortical region, pharmacological effects, and other contributors. Typically, CV ranges continuously from 0.2 to 3.0, transitioning from highly desynchronized to highly synchronized states. This indicates that CV, as a measure of spiking variability, can serve as a proxy of cortical state; in fact, CV has proven to be an excellent tool for data segmentation based on spiking variability. For instance, in work published by Fontenele *et al* (FONTENELE et al., 2019), CV was used to find criticality indicators between cortical states. In work done by Lotfi *et al* (LOTFI et al., 2020), maximum entropy methods were used to uncover signatures of brain criticality across cortical states. In line with these studies, we used CV as a data segmentation tool to access different cortical states in recordings from anesthetized rats and freely moving mice. Since the LFP data is measured independently of spiking activity, we were able to establish consistent relationships between LFP and CV using an information quantifier, which will be defined in the following chapter.

3 STATISTICAL COMPLEXITY

At its most basic level, a system is considered to have complexity if it does not exhibit patterns that can be deemed trivial. This concept may seem redundant, as intuition can often mislead our understanding of simplicity and complexity. For instance, consider a perfect crystal and an isolated ideal gas. The perfect crystal is completely ordered, with the arrangement of atoms adhering to strict symmetry rules. In this state, the probability of finding the system in such a symmetric arrangement predominates over all other accessible states, indicating that the information stored in the system is minimal. In contrast, the isolated ideal gas is entirely disordered, with all possible accessible states having equal probabilities of occurring. This means that the system contains maximum information. Despite representing extremes on the spectrum *order* and *information*, both systems serve as trivial models, and therefore, neither can be classified as complex.

Unfortunately, there is no universal definition of complexity, as various measures have been proposed over the decades, each tailored to the interests of specific fields. For instance, Kolmogorov's complexity (KOLMOGOROV, 1965; CHAITIN, 1977) is an algorithmic-information measure based on the smallest computer program capable of producing a given pattern. In contrast, Crutchfield and Young's complexity (CRUTCHFIELD; YOUNG, 1989) quantifies the amount of information about the past required to predict future states. Additionally, some measures focus on the self-organizing potential of systems (SPROTT, 2003). In this work, we will apply the Martin-Plastino-Rosso (MPR) statistical complexity (MARTIN; PLASTINO; ROSSO, 2006), which is rooted in the concept of statistical complexity proposed by López-Ruiz *et al.* (LóPEZ-RUIZ; MANCINI; CALBET, 1995), by using the Bandt-Pompe technique (BANDT; POMPE, 2002) to assign a probability distribution function to time series generated by the systems of our interest. The focus of statistical complexity are systems with intricate patterns hidden within their dynamics while themselves are simpler than their own dynamics. The MPR statistical complexity is an information based quantity, whose definition and analysis will be given in the following sections.

3.1 INFORMATION AND DISEQUILIBRIUM

An information measure $\mathscr{F}$ can be generally seen as a quantity that characterizes a system with multiple possible outcomes. In physical processes, information measures are usually given in term of entropies, which are uncertainty measures associated with systems described by a probability distribution function $P \equiv \{p_j; j = 1, 2, ..., N\}$.

Quantitatively, an information measure interpretation is straightforward, If $\mathscr{F}[P] = 0$ we can predict with certainty which of the N possible outcomes will take place, which translates into our *ignorance* of the system described by the distribution P being minimal. By contrast, when $\mathscr{F}[P] = max$ we have maximum *ignorance*, which happens when the probability distribution function is uniform, that is, when all states have equal probability $P_e = \{p_j = 1/N, \forall j = 1, 2, ..., N\}$.

Here, we define $\mathscr{F}$ in terms of the Shannon entropy, given by

$$\mathscr{F} \equiv S[P] = -\sum_{j=1}^{N} p_j \ln p_j, \tag{3.1}$$

which was first introduced in 1948, along the concept of information entropy, by Claude Shannon (SHANNON; WEAVER, 1949). It is usual to define the normalized quantity of the Shannon entropy in the fashion

$$H[P] = S[P]/S_{max}, \tag{3.2}$$

where $S_{max} = S[P_e] = \ln N$ and $0 \leqslant H[P] \leqslant 1$. The two extreme circumstances of minimal *ignorance* $H[P] = 0$ and maximum *ignorance* $H[P] = 1$ can be regarded as "trivial" ones, as neither contains the mixture of order and disorder present in complex systems. It follows that a definition of statistical complexity measure cannot be proposed with "information" alone. We can adopt a distance $\mathscr{D}$ from the uniform distribution P_e in order to define a "disequilibrium" Q as

$$Q[P] = Q_o \mathscr{D}[P, P_e], \tag{3.3}$$

where Q_o is a normalization constant so that $0 \leqslant Q[P] \leqslant 1$. The disequilibrium is different from zero when there are more likely states than others and is equal maximized when one of the states has probability equal to one. With this, we can define statistical complexity as a measure

that reflects the interplay between information stored in the system and its disequilibrium. Consequently, we adopt the following functional form for the statistical complexity measure:

$$C[P] = H[P] \cdot Q[P]. \tag{3.4}$$

There are many options we can use for the distance $\mathscr{D}$. Here we use the Jensen's divergence, defined by

$$J^{\beta}[P, P_e] = S\left[\beta P + (1-\beta)P_e\right] - \beta S[P] - (1-\beta)S[P_e], \tag{3.5}$$

with $0 \leqslant \beta \leqslant 1$ and $S[P_e] = \ln N$. We apply the special case of $\beta = 1/2$, so that

$$J^{\beta=1/2}[P, P_e] = J[P, P_e] = S\left[\frac{P + P_e}{2}\right] - \frac{1}{2}S[P] - \frac{1}{2}\ln N, \tag{3.6}$$

where $J[P, P_e]$ is equal to zero when $P = P_e$, and maximum when P is a one-point distribution that has the form

$$P_{one} = \begin{cases} 1 & \text{if } j = i, \\ 0 & \text{otherwise.} \end{cases} \tag{3.7}$$

A probability distribution of this form is the same that generates minimal *ignorance* of the system. Therefore, $S[P_{one}] = 0$ and J_{max} can be calculated by

$$J_{max} = J[P_{one}, P_e] = S\left[\frac{P_{one} + P_e}{2}\right] - \frac{1}{2}\ln N, \tag{3.8}$$

where

$$\frac{P_{one} + P_e}{2} = \begin{cases} \frac{N+1}{2N} & \text{if } j = i, \\ \frac{1}{2N} & \text{otherwise,} \end{cases} \tag{3.9}$$

and consequently,

$$S\left[\frac{P_{one} + P_e}{2}\right] = -\left(\frac{N+1}{2N}\right)\ln(N+1) + \ln(2N), \tag{3.10}$$

which results in

$$J_{max} = -\frac{1}{2}\left[\left(\frac{N+1}{N}\right)\ln(N+1) + 2\ln(2N) + \ln N\right]. \tag{3.11}$$

The disequilibrium associated with Jensen's divergence $Q[P, P_e] = Q_o J[P, P_e]$ is normalized when $Q_o = J_{max}^{-1}$ and its extremes are opposite to those of Shannon entropy. More specifically, if $P = P_{one}$ we are in a situation of perfect order ($H[P_{one}] = 0$) and maximum distance from the uniform distribution ($Q[P_{one}, P_e] = 1$), consequently, this scenario results in a system with no statistical complexity ($C[P_{one}] = 0$). Conversely, in a situation of complete randomness ($H[P_e] = 1$) and minimum distance from the uniform distribution ($Q[P_e, P_e] = 0$), we again observes that the system exhibits no statistical complexity ($C[P_e] = 0$).

The product form of statistical complexity $C = H \cdot Q$ implies that for a given value of normalized entropy H, the complexity C varies between a well defined minimum C_{min} and maximum C_{max} value, which restricts the possible occupied region in the complexity-entropy ($C - H$) plane. This occurs because, in PDFs with more than two possible states ($N > 2$), multiple distributions can yield the same entropy, even though each of these distributions may correspond to a different level of disequilibrium. In a later section, we will analyze this $C - H$ plane in more detail as various characteristics of the system can be inferred from the position on the plane.

3.2 BANDT AND POMPE TECHNIQUE

We have defined a measure of statistical complexity based on a system's entropy and disequilibrium, which are both derived from the system's probability distribution function. This yields a conceptual problem: *how do we calculate these quantifiers for an arbitrary series of observations* $\{t_1, t_2, t_3, ...\}$*?* For instance, in this work we aim to study LFP time series, which are real-world signals with high spatial-temporal resolution and has presence of dynamical noise. How can we derive a probability distribution function from these types of signals? To overcome this, we apply the *Bandt and Pompe* permutation entropy technique (BANDT; POMPE, 2002).

Let $X(t) \equiv \{x_t; t = 1, 2, ..., M\}$ be the time series representing a set of M measures of the observable X. We aim to associate to X, a probability distribution given by $P \equiv \{p_j; j = 1, 2, ..., N\}$ where $\sum_{j=1}^{N} p_j = 1$ and N is the number of possible states of the system. Here, we use a symbolic representation of a time series introduced by Bandt and Pompe for evaluating the probability distribution function (PDF) associated to each time series $X(t)$ of interest. This symbolization technique consists of extracting the ordinal patterns of length D, by indexing each time t to the D-dimensional vector $\mathbf{s}(t) = (x_t, x_{t+1}, \cdots, x_{t+D-1}, x_{t+D})$.

The specific $j-th$ ordinal pattern associated to $\mathbf{s}(t)$ is the permutation $\pi_j = (r_0, r_1, ..., r_{D-1})_j$

of $(0, 1, ..., D-1)$ which guarantees that $x_{t+r_0} \leqslant x_{t+r_1} \leqslant \cdots \leqslant x_{t+r_{(D-2)}} \leqslant x_{t+r_{(D-1)}}$. In other words, each permutation π_j (with $j = 1, 2, ..., D!$) is one of our possible symbols and we have $D!$ different symbols (ordinal patterns). To calculate the PDF we should identify and count the number of occurrences of each symbol π_j of length D.

This procedure is essential to a phase-space reconstruction with embedding dimension (pattern length) D. Higher values of D yield a more precise probability distribution function (PDF) but require greater computational effort, as increasing D necessitates larger time series windows. For practical purposes, Bandt-Pompe suggested to use $3 \leqslant D \leqslant 7$. Note that the probabilities to evaluate the PDF naturally arises from the time series after defining the symbols. This technique takes into account the temporal structure of the time series and yields information about the temporal correlation of the system.

Figure 16 – Characterizing the symbolic representation of time series. (a) The six possible symbols associated with permutations π_j for the case of embedding dimension $D = 3$. (b) example of a simple time series $X(t)$ and (c) its non-normalized probability density function.

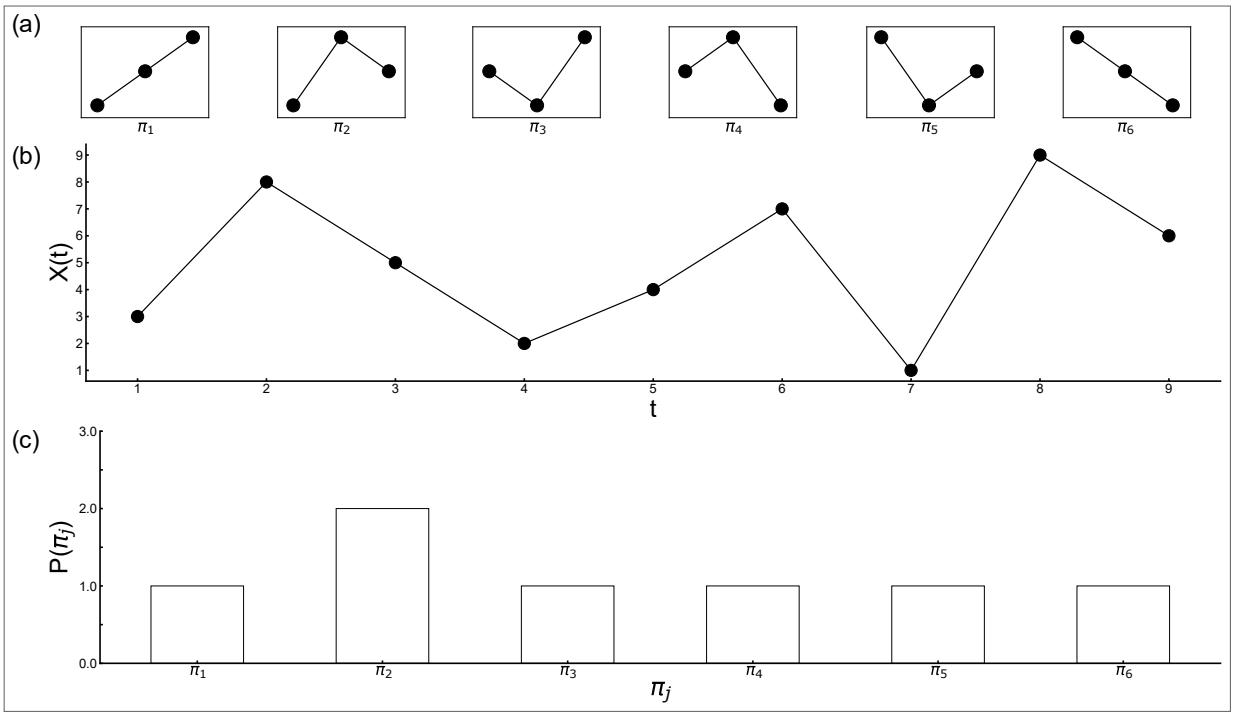

Source: adapted from LOTFI et al. (2021)

To have an example, choosing $D = 3$, all the $j = 6$ possible symbols associated with the permutations π_j are: $\pi_1 = (0, 1, 2)$, $\pi_2 = (0, 2, 1)$, $\pi_3 = (1, 0, 2)$, $\pi_4 = (1, 2, 0)$, $\pi_5 = (2, 0, 1)$, $\pi_6 = (2, 1, 0)$. These are visually shown in Fig. 16(a). Considering an illustrative time series $X(t) = \{3, 8, 5, 2, 4, 7, 1, 9, 6\}$, shown in Fig. 16(b), the first vector is $\mathbf{s}(t = 1) = (3, 8, 5)$, corresponding to the permutation $\pi_2 = (0, 2, 1)$; the second vector is $\mathbf{s}(t = 2) = (8, 5, 2)$,

corresponding to to the permutation $\pi_6 = (2, 1, 0)$; the third vector is $\mathbf{s}(t = 3) = (5, 3, 4)$, corresponding to the permutation $\pi_5 = (2, 0, 1)$. Similarly, one can find the other 4 vectors $\mathbf{s}(t)$ and their respective π_j in order to build the PDF associated to $X(t)$. The correspondent non-normalized PDF is shown in Fig. 16(c).

It is also possible to include a time delay τ to evaluate the PDF in different time scales. This means that we can skip every $\tau - 1$ points of our time series $X(t)$ in order to find and count the symbols. In the example used above (Fig. 16) we use $\tau = 1$ and consider every point in $X(t)$. For $\tau = 2$ we would skip every other point in such a way that the first vector is $\mathbf{s}(t = 1) = (3, 5, 4)$, corresponding to the permutation $\pi_2 = (0, 2, 1)$; the second vector is $\mathbf{s}(t = 2) = (8, 2, 7)$, corresponding to the permutation $\pi_5 = (2, 0, 1)$; the third vector is $\mathbf{s}(t = 3) = (5, 4, 1)$, corresponding to the permutation $\pi_6 = (2, 1, 0)$. For $\tau = 3$ the first vector is $\mathbf{s}(t = 1) = (3, 2, 1)$, the second vector is $\mathbf{s}(t = 2) = (8, 4, 9)$; the third vector is $\mathbf{s}(t = 3) = (5, 7, 6)$. Therefore, to each time series $X(t)$ we can associate many PDFs, each one for a different value of the time delay τ.

By using the Bandt and Pompe technique, we can assign a probability distribution to any signal. However, it is important to understand the implications of this distribution in relation to the signal itself. Since the method considers the permutations of how the signal changes, the distributions do not provide information about the actual values of the signal but rather about how strongly the signal is auto-correlated within specific time frames. For instance, considering $D = 3$, which yields 6 possible permutations, if the probability distribution is equally distributed between these permutations, such that $P(\pi_j) = 1/6$, it indicates that no intrinsic dynamics are observed in the signal. In this case, the changes can be regarded as noise, resulting in high entropy. Conversely, if only one permutation is present in the signal, leading to zero entropy, it implies that no significant statistical information is found, as the signal changes in a consistent manner. Therefore, this technique is particularly relevant for analyzing signals that exhibit considerable noise while also possessing underlying dynamics that drive the signal.

3.3 ANALYZING THE C-H PLANE

Now that we are able to derive a probability distribution function (PDF) from any real-world time series by using Bandt and Pompe symbolization technique, we can calculate the statistical complexity and Shannon entropy for such time series using Eqs. 3.1 and 3.4. However, what

can we infer about the dynamical systems that generate these time series from the $C - H$ plane?

Originally, the complexity-entropy plane was proposed by O. Rosso and co-authors with the intent to distinguish noise from chaotic dynamics (ROSSO et al., 2007). They observed that chaotic systems typically exhibit entropies ranging from 0.45 and 0.75, with complexities approaching their maximum due to the presence of correlated structures. In contrast, time series dominated by white noise demonstrate maximum entropy, as expected, while exhibiting minimum complexity. As correlation is introduced into the noise, systems tend to position themselves within regions characterized by medium complexity and entropy. On the other hand, more deterministic systems, such as regular oscillations, are found in areas with both low entropy and low complexity. Fig. 17 provides a graphical representation of these regions, utilizing an embedding dimension of $D = 6$.

It is important to note that the representation depicted in Fig. 17 is prototypical. This means that the interpretation and position of a dynamical system in the $C - H$ plane will depend on the characteristics of the associated time series. For instance, consider a system exhibiting stochastic oscillations observed with a sampling rate closely matching the natural frequency of the dynamics. In this case, the position in the plane would fall in the bottom right corner, as the time series would be perceived as noise. On the other hand, if a very high sampling rate is employed, the time series would exhibit high auto-correlation, positioning it in the bottom left of the plane. Thus, merely changing the temporal scale of the series can reveal complex behaviors within the plane.

Statistical complexity is useful for analyzing complex systems and detecting patterns or changes in the system's dynamics over time. It can also be used to compare different dynamic systems and see if they exhibit similarities or differences in terms of entropy and complexity. In neuroscience, permutation entropy and statistical complexity have been used to investigate different brain signals under different contexts. In EEG data, they have been used to distinguish cortical states (ROSSO et al., 2006), to characterize sleep stages (MATEOS; GóMEZ-RAMíREZ; ROSSO, 2021), to study epilepsy, coma, anesthesia (MATEOS; DIAZ; LAMBERTI, 2014; ZHU et al., 2019; JORDAN et al., 2008). In MEG data, it has been used to reveal different dynamics in cortical activity using different frequency bands (MENDOZA-RUIZ et al., 2020). It has been applied to monkey LFP to estimate response-related differences between Go and No-Go trials (LUCAS et al., 2021), to estimate time differences during phase synchronization (MONTANI et al., 2015), and more recently to explore Hénon map as a model for brain dynamics based

Figure 17 – Graphical representation of the $C - H$ plane proposed by O. Rosso and co-authors. Maximum (C_{max}) and minimum (C_{min}) complexity bounds are shown using Shannon entropy and statistical complexity of a time series using embedding dimension of $D = 6$. Chaotic behaviour is located towards the maximum complexity with entropies between 0.45 and 0.75. Systems with dynamical correlated noise are represented in the middle and trivial systems composed of purely white noise and regular oscillations are also shown.

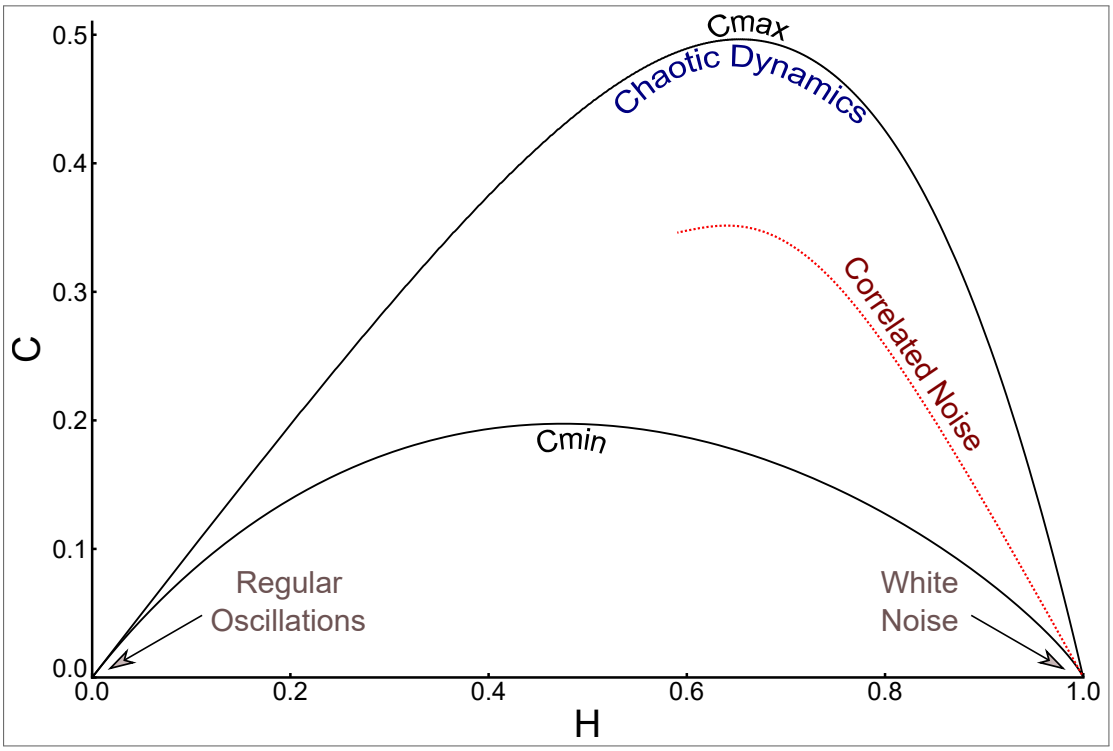

Source: the author.

on LFP data from subthalamic nucleus (STN) and medial frontal cortex (MFC) of human patients (GUISANDE et al., 2023).

Work on statistical complexity with spiking activity has also been done by Lofti *et al* (LOTFI et al., 2021). In this research, MPR statistical complexity calculated using a permutation entropy was performed for firing rate signals of seven urethane anesthetized rats, windowed by the spiking variability. More specifically, using a bin of $20 - 50ms$, the firing rate of neuron populations was segmented into 10-seconds windows, with the CV being calculated for each window and, consequently, the statistical complexity and Shannon entropy was calculated for different cortical states. The experimental methodology of the surgery recordings used was the same as the one performed in the urethane anesthetized rats of this work.

Fig. 18(a) shows the group data of both information quantifiers, entropy and statistical complexity, of firing rate signals as a function of spiking variability (CV), as well as, the corresponding complexity-entropy ($C - H$) plane. Group data of all seven animals is presented as dashed lines and colored markers represent results of individual rats. Note that the Shannon

Figure 18 – Information-theory quantifiers of spiking rates for different levels of spiking variability of the cortical states for 7 rats. (a) The Shannon entropy (top) and statistical complexity versus CV are presented for each rat and as a group average (dashed line) as well as the $C-H$ plane. The complexity peaks at $C_{max} = 0.333 \pm 0.001$ for $H_{C_{max}} = 0.70 \pm 0.05$ and $CV_{C_{max}} = 1.35 \pm 0.15$.(b) Statistical complexity versus CV (top) and the $C - H$ plane (bottom) calculated from simulations of a network model (blue dots), compared to the group average (black line) of the 7 rats in (a). Firing rates were analyzed with the same protocol in both cases.

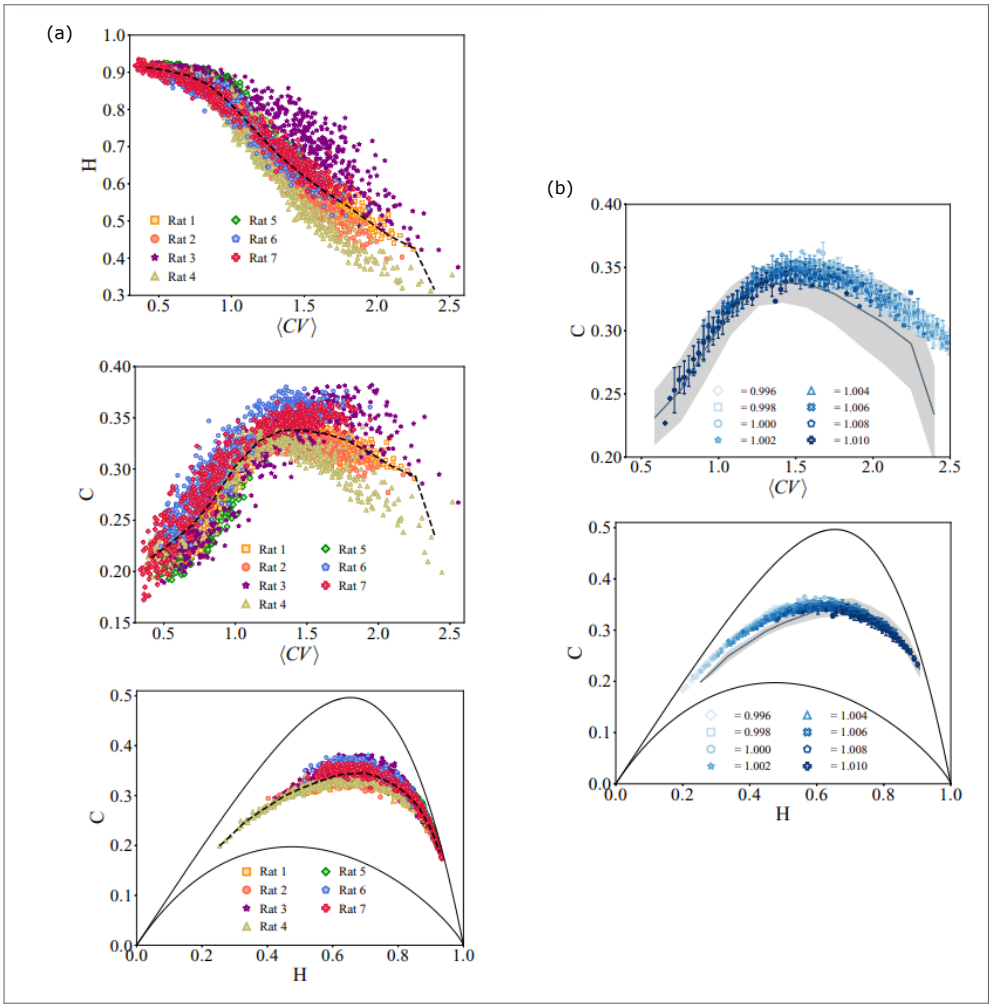

Source: adapted from LOTFI et al. (2021)

entropy decreases monotonically with CV, which indicates that for low values of CV (desynchronized state) the firing rate functions as a very noisy signal, yielding a high entropy. As CV increases and the cortical state becomes more synchronized, the firing rate signals appear as localized bursts, which consequently, lowers an entropy based on permutation. These situations are extremes in terms of entropy, however, their complexities are not, as we can see in the $C - CV$ results. The firing rates have peaks in their complexities when at intermediaries CV, suggesting a more complex dynamics of firing rates under states of mixed synchrony and desynchrony of spiking data. Curiously, this peak, for the group data, occurs at $CV_{C_{max}} = 1.3 \pm 0.1$, which coincides with the CV range where scaling relations between

the power laws exponents of spike avalanches were found in previous work (FONTENELE et al., 2019). The $C - H$ plane of these firing rates shows that these signals have a wide range of intrinsic dynamics patterns, with a peak of complexity ($C_{max} = 0.333 \pm 0.001$) for a relatively high entropy ($H_{C_{max}} = 0.70 \pm 0.05$), and this was true for all rats.

Building on their findings related to criticality, Lofti *et al* extended their analysis to a probabilistic cellular automata network model,where the critical point was clearly defined (KINOUCHI; COPELLI, 2006). They applied the same methods of permutation entropy and statistical complexity to the simulated firing rates of this model, varying a control parameter within the criticality region. alongside the group data results from living animals, represented by solid lines with shaded areas indicating standard deviation. The blue markers represent the simulation results for different control parameters, complete with their respective error bars. Notably, the simulation results closely resemble those observed in living rats.

This work was inspired by the statistical complexity results derived from spiking data and serves as a natural extension of those findings. We applied permutation entropy and MPR statistical complexity to local field potential (LFP) data from anesthetized rats and freely moving mice, segmenting the data based on cortical states defined by spiking variability. The results obtained from the LFP signals were non-trivial and significantly different from those derived from firing rates. This provided a unique perspective for analyzing these quantifiers in the context of LFP data and exploring the relationship between spiking activity and LFP.

4 STATISTICAL COMPLEXITY OF LFP IN THE PRIMARY VISUAL CORTEX

Deep layers of pyramidal neurons in rodents' primary visual cortex have dendrites reaching all six layers, making them important integrators in the cortical column (SHAI et al., 2015). We already investigated its complexity based on its spiking activity (LOTFI et al., 2021). However, an analysis of the statistical complexity of local field potential in deep layers of V1 is still lacking, especially when observed along multiple cortical states. Fig. 19 (a) displays an illustration of details for a pair of shanks of the silicon probe (Buzsaki64sp, Neuronexus) used to record six local neuronal populations, 200 $/mu$m apart.

Here we associate different cortical states with different levels of summed spiking variability in large neuronal populations (RENART et al., 2010; HARRIS; THIELE, 2011; VASCONCELOS et al., 2017; FONTENELE et al., 2019; LOTFI et al., 2020; LOTFI et al., 2021). Fig. 19 (b) displays the time-series of the coefficient of variation CV, calculated over non-overlapping 10-s-long windows, illustrating the summed spiking variability within neuronal populations in V1 of urethane-anesthetized rats. In addition, its right panel displays the corresponding CV histogram. Fig. 19 (c) illustrates the detailed spiking activity across the same neuronal population in its different levels of summed spiking variability, according to the corresponding colored markers in (b): low (blue), intermediate (green), high (red). The spiking activity of each SUA and MUA is shown along a time window of 10s in a binary form. This means that if a dot is colored, then a spike of that unit was registered at that instant, if it's white, then that unit was at silence at that instant. The top panels in Fig. 19 (c) show the firing rate calculated in a time window of 50 ms. The bottom panels show the raster plots of 90 single-units and 145 multi-units activity in the vertical axis. Each dot represents a spike.

Fig. 19 (d) shows samples of 10-s-long local field potentials along the different levels of summed spiking variability shown in (b) (using the same color code), whereas the Fig. 19 (e) shows the corresponding power spectrum density (PSD) of LFP signals. At low CV, the spiking activity is desynchronized and the LFP power spectrum is relatively flat. At intermediate CV, the spiking activity becomes more synchronized. At high CV, the spiking activity is highly synchronous and the LFP power spectrum is dominated by low frequencies. This is similar to previous report by Hahn *et al* (HAHN et al., 2017), where they found that the variability of cortical dynamics can be characterized by different cortical states based on the frequency composition of the LFP power spectrum. In this work, they were able to relate low frequency

peaks of LFP with criticality.

Figure 19 – Cortical dynamics in different levels of spiking variability. (a) Schematics of silicon probe (6 shanks) inserted in the rat's primary visual cortex (V1). (b) Coefficient of variation (CV) of spiking activity calculated for 10-s-long non-overlapping windows, followed by the CV histogram of a single animal; Symbols (blue circle, green square, and red triangle) indicate the level of spiking variability of three representative examples: low (CV$= 0.42$, desynchronized activity), intermediate (CV$= 1.04$), and high (CV$= 2.03$, highly synchronous activity). (c) Spiking activity across the three levels of CV depicted in (b). (Top) Firing rate calculated using 50 ms bin. (Bottom) Raster plots of single- and multi-units activity (SUA$= 90$ and MUA$= 145$). (d) 10-s-long LFP data across the three levels of CV. LFP is tracked using 500 Hz sample rate and a low-pass Butterworth filter is applied with cutoff frequency of $f_{cutoff} = 200$ Hz. (e) Power spectrum density (PSD) of data shown in (d).

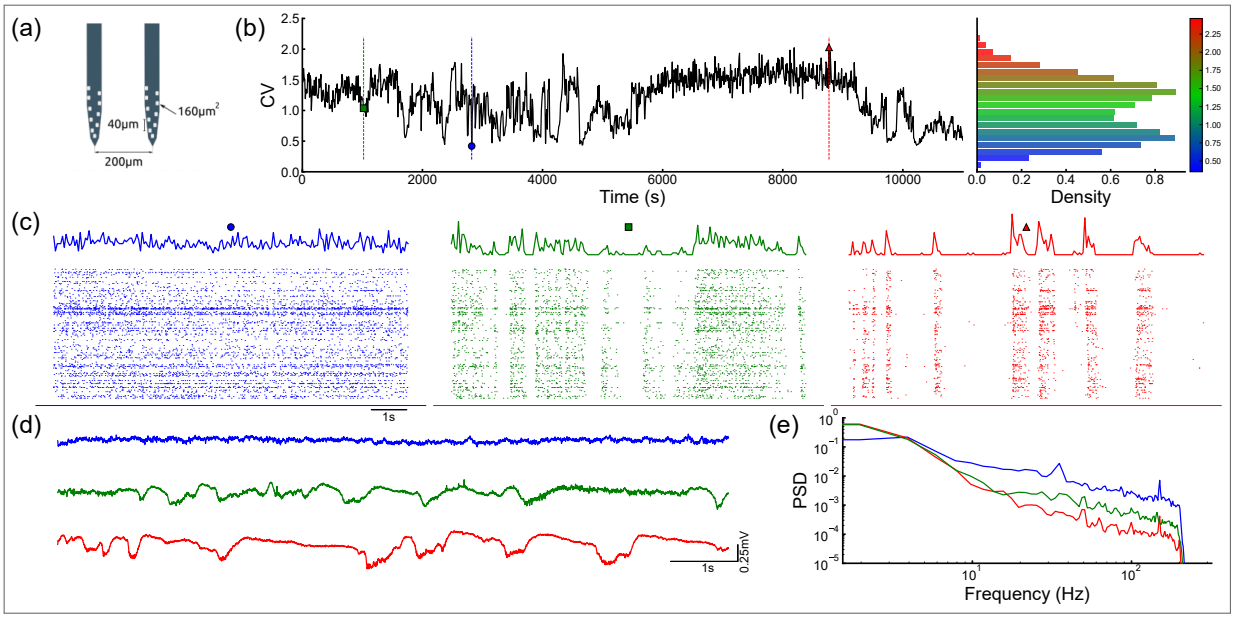

Source: from JUNGMANN et al. (2024)

4.1 STATISTICAL COMPLEXITY IN ANESTHETIZED RATS

With the aim to find quantitative and consistent relations between LFP and spiking activity, we investigated the statistical complexity and Shannon entropy of LFP across multiple cortical states characterized by spking patterns. Fig. 20 (a) shows the statistical complexity of 10-s-long windows of LFP data versus the time delay τ calculated for each shank (dashed lines) for multiple levels of variability in population spiking activity (low CV in blue and high CV in red). The average (lines) and standard deviation (shading) are calculated based on all shanks. The complexity correlation matrix of all 6 shanks for low and high CV, which measures the correlation between the time series of the statistical complexity calculated in different shanks of the same experimental setup, is also shown. Fig. 20 (b) shows the statistical complexity (left) and Shannon entropy (middle) of LFP versus CV of the spiking activity for $\tau = 200$ ms.

The average group data (black circles) and standard deviation (blue shading) are taken over all shanks of a single animal using bins of 0.02 s for the CV axis. Complexity and entropy plane (right) are represented using group average. Black lines represent the theoretical maximum C_{max} and minimum C_{min} complexity values in the $C - H$ plane for $D = 6$.

These results show that the statistical complexity of the LFP increases with increasing CV (peaking at $C = 0.4$), with a more pronounced effect for higher time delays τ. This suggests that the LFP becomes less noisy with increasing spiking variability, which is expected for more synchronized regimes. Even at very large CV, where the LFP's spectrum is composed mainly of very low frequencies, we find LFP signals with high complexity. This is quite interesting, since previous report of statistical complexity based on its spiking activity (LOTFI et al., 2021) found a maximum of complexity in windows of mid-range CV and a low complexity for both high and low CV. This bring to the surface, just how different these signals, firing rate and LFP, are from each other, even when analyzed in the same time window. The complexity correlation matrix also shows that the LFP signals across different shanks become more correlated with increasing spiking variability. This could be related to recent discussions on the local range of LFP signals (KAJIKAWA; SCHROEDER, 2011; HERRERAS, 2016). This might indicate that LFP signals composed mainly of low frequencies have longer spatial reach compared to signals with an abundance of high frequencies. The Shannon entropy of the LFP decreases with increasing CV (from the maximum to close to 0.7), although the effect is less pronounced than for the statistical complexity. This suggests that the LFP becomes more predictable with increasing spiking variability.

The diverse group data based on all urethane-anesthetized rats, male/female, albino/non-albino (please refer to methods for more details) is shown in Fig. 20 (c). Group average (black circles) and standard deviation (blue shading) are taken over all 42 shanks of all 7 rats using bins of 0.02 s for the CV axis. The average of each animal is also presented (colored markers). Qualitatively, results are the same for each rat: increasing relation between the statistical complexity of the LFP and CV (left) and inverse relation between the Shannon entropy of the LFP and CV (middle). The $C - H$ plane (right) suggests the maximum values achieved of complexity are associated with the minimum values achieved of entropy which both occur for higher spiking variability (CV ≥ 1.5). Overall, the results suggest that the statistical complexity and Shannon entropy of the LFP are both sensitive to changes in spiking variability, with the complexity being maximized in high CV windows, where the LFP has a dominant presence of low frequencies bands. This suggests that these measures could be used to assess changes in

the dynamics of cortical circuits.

Figure 20 – Complexity and entropy quantifiers across different levels of spiking variability. (a) (left) Statistical complexity of 10-s-long windows of LFP data versus the time delay τ calculated for each shank (dashed lines) for low (blue) and high (red) CV. Average (lines) and standard deviation (shading) is performed over all shanks. (right) Complexity correlation matrix of all 6 shanks for low and high CV. (b) Statistical complexity (left) and Shannon entropy (middle) of LFP versus CV of the spiking activity for $\tau = 200$ ms. Group average (black circles) and standard deviation (blue shading) is taken over all shanks using bins of 0.02 for the CV axis. Complexity and entropy plane (right) is represented using group average. Black lines represent the theoretical maximum C_{max} and minimum C_{min} complexity values in the $C - H$ plane for $D = 6$. (c) Group data for corresponding plot in (b), from primary visual cortex of 7 animals, in 42 local neuronal populations.

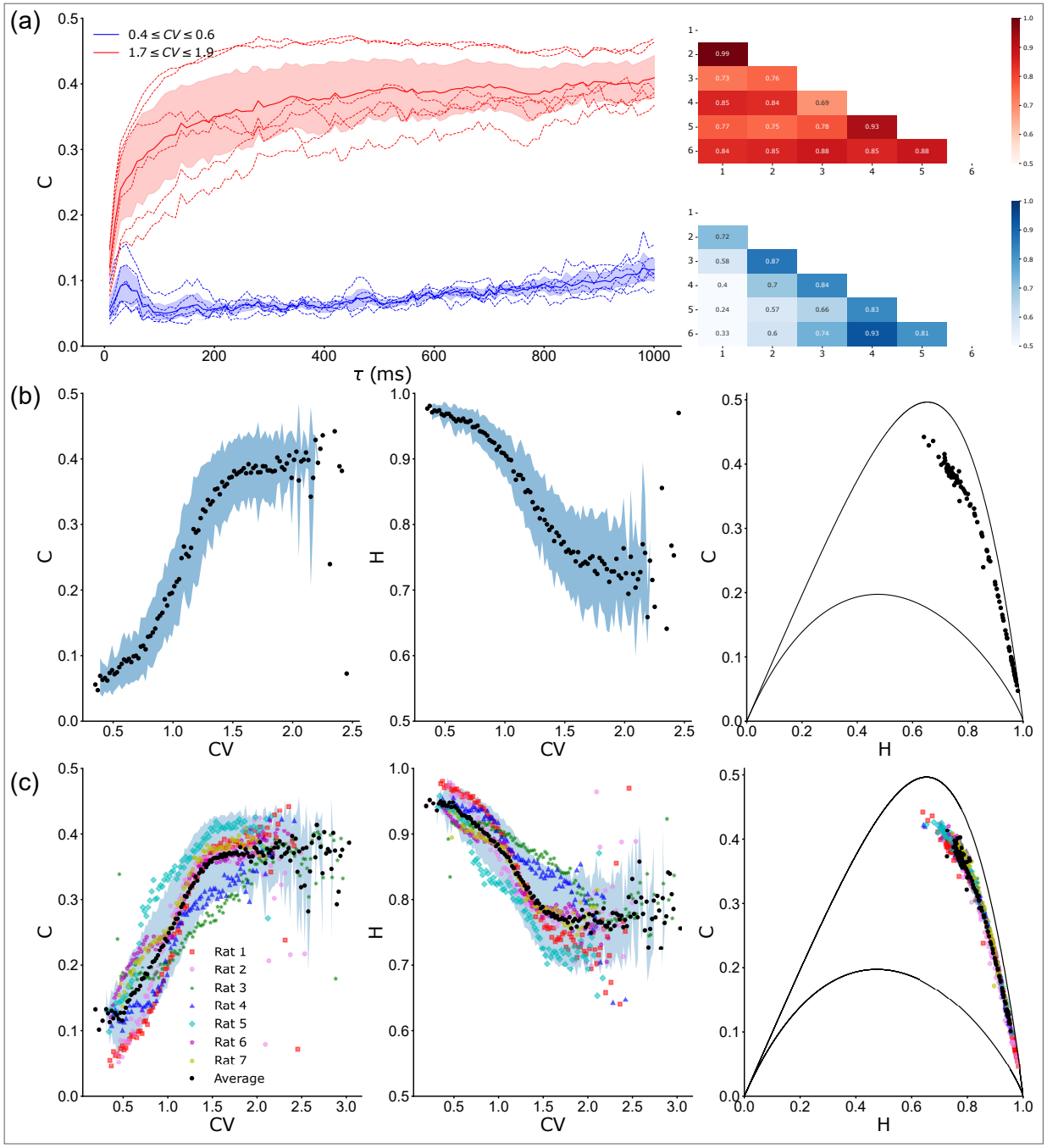

Source: from JUNGMANN et al. (2024)

In these shown results, we used $D = 6$ to achieve a high number of different LFP states. However, we also performed analysis for $D = 4$ and $D = 5$, yielding results qualitatively similar to those for $D = 6$. This can be seen in Fig. 21 (a), where we provide the group average of the statistical complexity and Shannon entropy of LFP versus CV of the spiking activity for $\tau = 200$ ms, varying D from 4 to 6. We see that complexity increases with CV for all D in a similar sigmoid-like curve, however the maximum value achieved decreases for smaller D. Similarly, the Shannon entropy decreases with CV for all D, reaching its minimum value for higher D. The decrease in the maximum values of the complexity by using smaller D is expected in a signals such as LFPs, since they have presence of many frequencies bands as well as noise, therefore, with less possible permutations, we would loose aspects of specific bands.

Additionally, to ensure the results are robust in terms of potential biases due to finite samples, we have performed the analysis using cut sections of the original data. Fig 21 (b) shows the group average of statistical complexity and Shannon entropy of the LFP versus the CV of spiking activity for $\tau = 200$ ms, using the original dataset, as well as versions of the data truncated by removing the final portion of the series to retain half and a quarter of the original dataset, with $D = 6$."We see that complexity (entropy) increases (decreases) with CV for all cases. The main conclusions do hold firm when removing half of the data in each window, however as $3/4$ of the data is removed from the windows, the results for low CV present fluctuations due to finite sampling. This happens because in low CV, the entropy is very high, which means that the LFP-state probabilities are close to a uniform distribution. Therefore, the 720 different LFP-states must be well sampled to correctly reproduce this uniform distribution. The original data, however, has well sampled LFP-state probabilities. All averages and standard deviation taken in Fig. 21 are taken over 42 local neuronal populations from primary visual cortex of 7 animals, using bins of 0.02 s for the CV axis.

Figure 21 – Group average of the statistical complexity (left) and Shannon entropy (right) of LFP versus CV of the spiking activity for $\tau = 200$ ms, using (a) $D = 4$ (green), $D = 5$ (red), $D = 6$ (blue), and (b) original data (blue), half of original data (red) and a quarter of original data (green) for $D = 6$. Averages (colored circles) and standard deviations (colored shadings) are taken over 42 local neuronal populations from primary visual cortex of 7 animals, using bins of 0.02 for the CV axis.

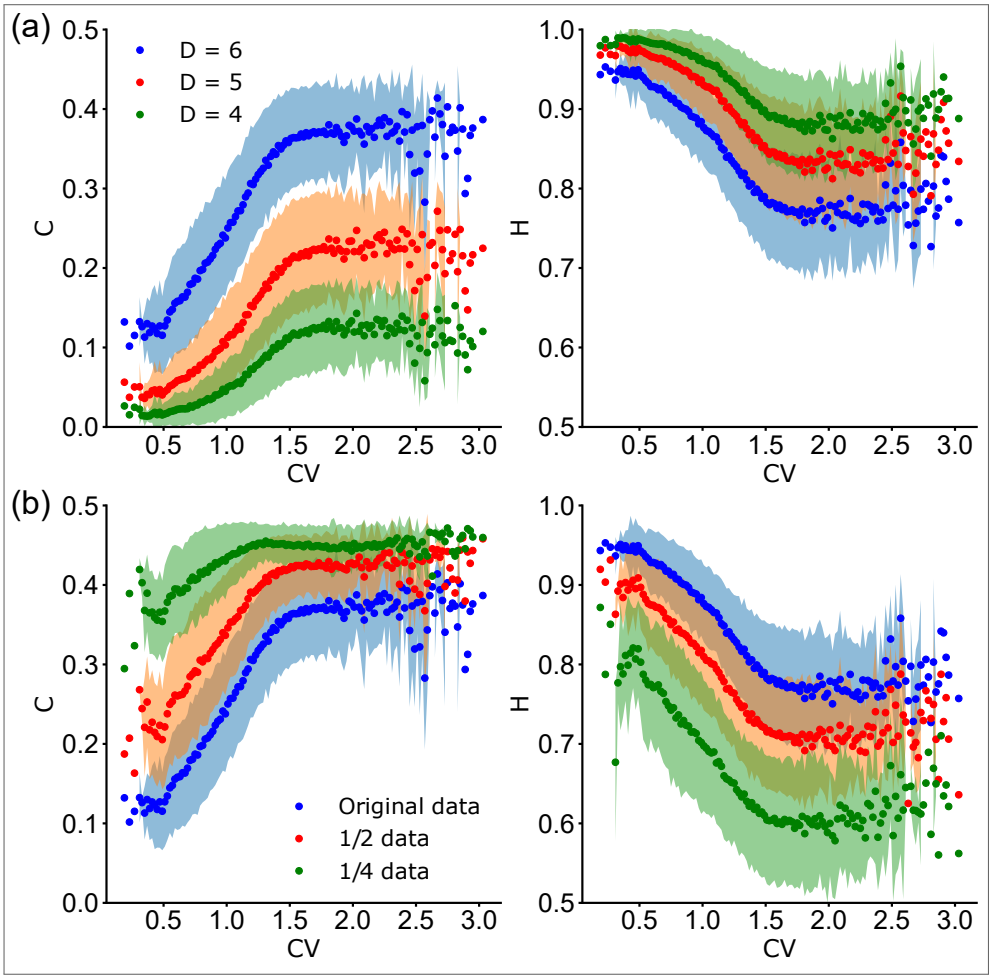

Source: from JUNGMANN et al. (2024)

4.2 STATISTICAL COMPLEXITY IN FREELY MOVING MICE

4.2.1 Complexity in layers

Previous studies have shown that the laminar structure of spontaneous and sensory-evoked population activity in mammals primary sensory cortex are related to the local information processing and the flow of information through cortical circuits (SAKATA; HARRIS, 2009; SENZAI; FERNANDEZ-RUIZ; BUSáKI, 2019; LIU et al., 2022). Therefore, we also calculated the statistical quantifiers along the laminar axis (dorsal-ventral axis) for freely moving mice.

Fig. 22 illustrates the depth profile of complexity and entropy quantifiers of the presynaptic

activity along the cortical states in the primary visual cortex of freely moving mice. As in the previous subsection, the cortical states were characterized by the level of spiking variability on the local summed population activity using the CV. In Fig. 22 (a), we examined the statistical complexity and entropy of 10-second-long windows of local field potential data as a function of the time delay τ. We calculated these measures across different channels, denoted by dashed lines, for two distinct conditions: low spiking variability, represented by the blue lines, and intermediate spiking variability, depicted by the red lines.

To ensure statistical robustness, we average the results (solid lines) and provide the standard deviation of the mean (shaded areas) over nearby channels (approximately 100 $/mu$m) within V1. Fig. 22 (b) provides a visual representation of the vertical silicon probe used to record the neuronal data from freely moving mice (SENZAI; FERNANDEZ-RUIZ; BUSáKI, 2019). The adoption of such a probe provided us with LFP data at varying depths in the mouse's V1, and we analyzed the corresponding complexity and entropy measures along these depths. In Fig. 22 (c), we focus on the relationship between the complexity and entropy of LFP data and their normalized depth. We adopted $D = 6$, and $\tau = 200$ ms and again considered low (blue) and medium (red) variability conditions. The dashed lines represent the average quantifier values, while the shaded regions indicate the standard deviation of the mean. Importantly, our analysis encompasses data from seven different mice, allowing us to derive general trends. We particularly highlight the significance of mid-layer 5 (denoted by the black star), which is presented as an average across all mice, shedding light on the neural dynamics at this specific depth.

Our findings indicate that, for larger time delays ($\tau > 100$ ms), there is a clear distinction in the statistical complexity and entropy of freely moving mice LFP under multiple levels of spiking variability, as in the case of anesthetized rats. In addition, a maximization of the statistical complexity is found in mid-layer 5 as we increase CV. The entropy appears to be the minimum for this depth when the CV is increased. These results are quite beautiful and unexpected, since this is derived from data of the primary visual cortex, a sensory related region. In sensory cortex, the layers $2/3$ are usually regarded as the critical layers in processing sensory information. Layer 4 it's a densely neuron packed layer where signals from the thalamus is integrated and conveyed to more superficial layers. Layer 5 is known for the larger pyramidal cells with significant multi-layer dendritic branching, so the maximum of complexity of the LFP in this layer is enigmatic. Perhaps, at higher CV windows, the LFP has a higher spatial reach and the maximization of the complexity reflects the integration of synaptic effects of all

layers in the soma layer 5 cells. However, further study is still necessary to answer this, as this maximum could be result from a geometrical aspect of the electrodes placement.

Note that the maximum values achieved by the CV of freely moving mice is lower than those of anesthetized rats, mainly due to anesthesia inhibition effects, not achieving values higher than $C = 1.3$. However, if we analyze Fig. 20 (b) in this region of CV, we see that the complexity values of anesthetized rats are similar to those of sleeping mice, being close to $C = 0.2$. This suggests that, for CV ≤ 1.3 and $\tau \geq$ 100ms, the results from anesthetized rats and freely moving mice are qualitatively similar.

Figure 22 – Depth profile of complexity and entropy quantifiers across different levels of spiking variability. (a) Statistical complexity and entropy of 10-s-long windows of LFP data versus the time delay τ calculated for different channels (dashed lines) for low (blue) and medium (red) CV. Average (lines) and standard deviation (shading) is performed over close by ($\approx$ 100 μm) channels in the mouse's V1. (b) Vertical silicon probe illustration. It contains 64 channels with 20 μm gaps between each site. (c) Complexity and entropy of LFP data versus normalized depth (layer 1 is marked as zero for each mouse) for low (blue) and medium (red) CV for $\tau = 200$ ms. Quantifier's average (colored dashed lines) and standard deviation (shading) is calculated using all 7 mice. Mid-layer 5 (black star) is represented as an average over each mouse.

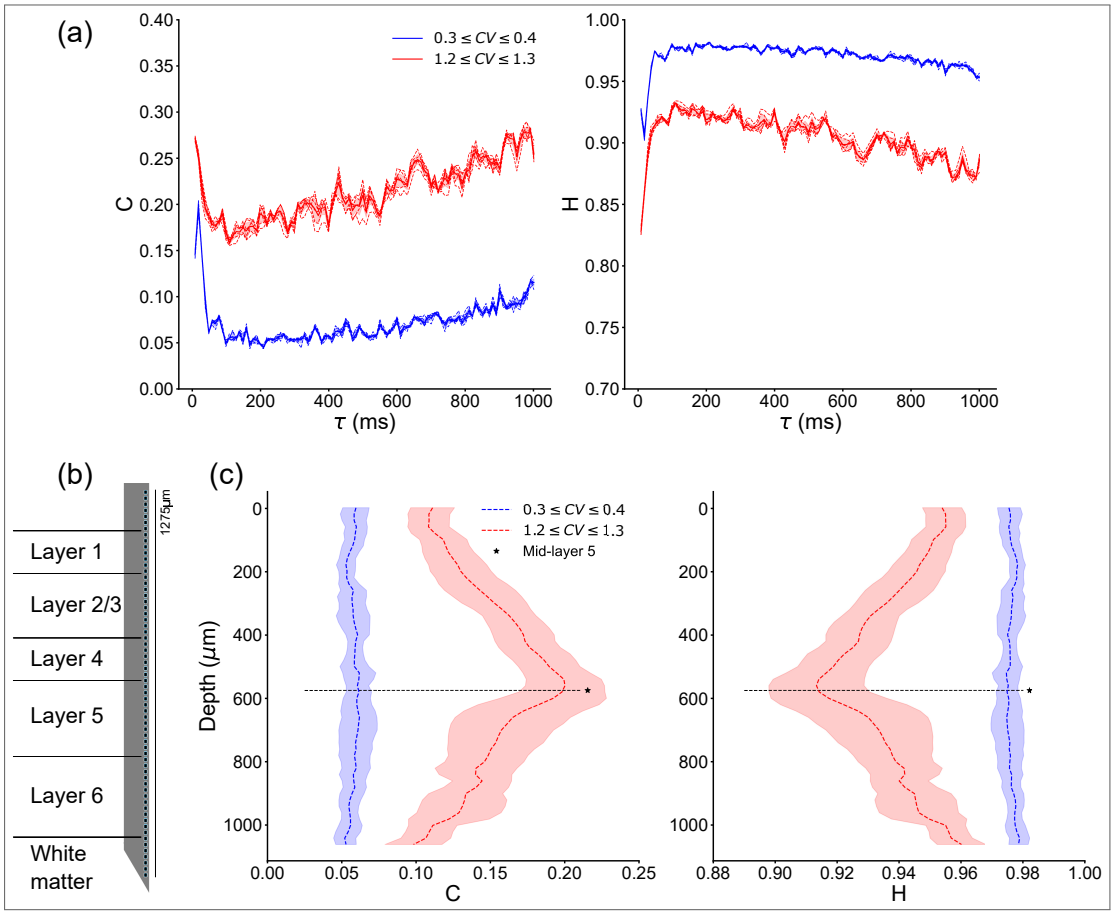

Source: from JUNGMANN et al. (2024)

4.2.2 Complexity across behavioral states

Sensory responses can be influenced at both neural and behavioral levels (MCGINLEY et al., 2015). For example, in recent decades researchers delved into the intricacies of the wake-sleep cycle, a fundamental phenomenon exhibited by all higher vertebrates. They aimed to unravel the underlying neuronal mechanisms governing this cycle, employing intracranial local field potentials recorded from various brain regions, including the cortex, hippocampus, striatum, and thalamus (GERVASONI et al., 2004; RIBEIRO et al., 2010). Therefore, we also estimate the information quantifiers using behavioral states of the freely moving mice as parameters for data segmentation. Fig. 23 shows the statistical complexity and entropy plane $C - H$ of V1's layer 5 LFP data along different behavioral states: NREM (non-rapid eye movement), REM (rapid eye movement), and awake which are represented by triangle, square, and circle markers, respectively. We have examined over 1900 NREM, 220 REM, and 1300 awake 10-s-long episodes using $D = 6$ and $\tau = 200$ ms, presenting the results as averages over all 7 mice. Fig. 23 suggests that the statistical complexity of the LFP achieves higher values in NREM states and, in contrast, lower values when the mouse is awake. REM states, on the other hand, appear to be associated with intermediary values of complexity. These results not only show that statistical complexity can be used as markers of behavioral state, but it also find a statistical difference between REM and wake states, which is particularly hard to do in cortical areas by just analyzing the PSD, and moreover, this difference can only be found in the complexity axis, as the error bars overlap in the entropy axis.

Since the LFP of NREM episodes is composed dominantly by lower frequencies, in contrast to rem and awake states, results from Fig. 23 corroborates with those segmented by CV, since LFP of high CV windows are also dominated by low frequencies. This suggests indirect links between CV of spiking activity and behavioral states.

Figure 23 – Entropy-complexity plane $C - H$ of V1's layer 5 LFP data along different behavioral states. These are NREM (triangle), REM (square) and awake (circle), where the marker indicates the corresponding mean value for each behavioral group in 10-s-long episodes of NREM, REM, and awake states for all 7 mice; where $D = 6$ and $\tau = 200$ ms; both complexity and entropy values were significantly different among behavioral groups (p$\ll$ 0.01, Mann-Whitney test).

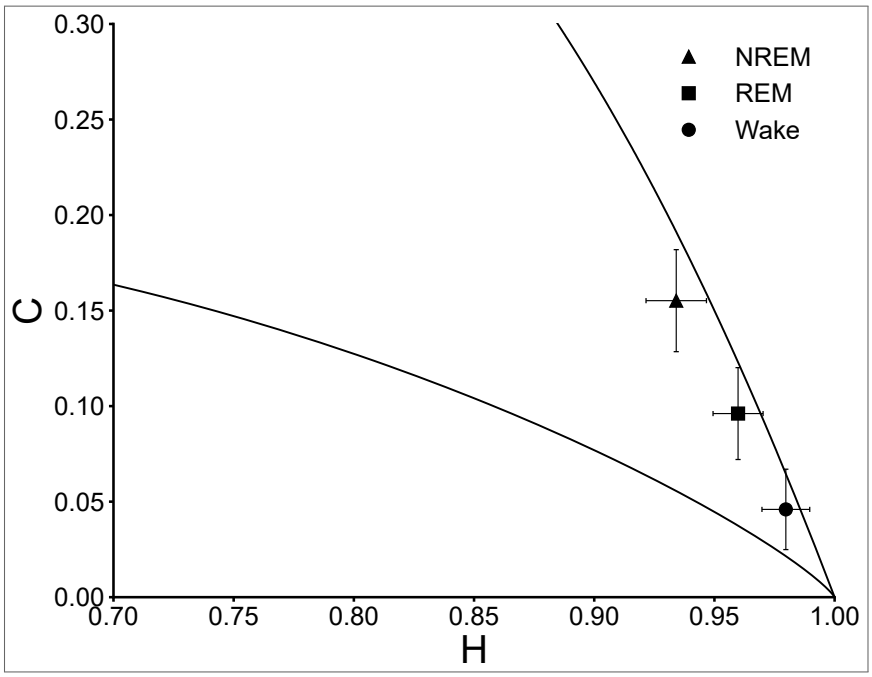

Source: from JUNGMANN et al. (2024)

5 CONCLUSIONS

This work addresses the gap between quantifiers of local field potentials (LFP)—specifically, complexity and entropy—and proxies of cortical state, such as the coefficient of variation (CV) of spiking activity. We have demonstrated that LFP data can be characterized using information-theoretic quantifiers: Shannon entropy (SHANNON; WEAVER, 1949) and Martin-Plastino-Rosso statistical complexity (MARTIN; PLASTINO; ROSSO, 2006). To achieve this, we employed a symbolic representation, based on Bandt-Pompe technique (BANDT; POMPE, 2002), allowing us to assign a probability distribution function to the LFP signals generated by urethane-anesthetized rats and freely moving mice.

The results of this study demonstrate that the statistical complexity and Shannon entropy of local field potentials (LFPs) in the deep layers of the primary visual cortex (V1) consistently vary with the level of summed spiking variability. At low coefficient of variation (CV), the cortical state exhibits desynchronized spiking activity, resulting in noisier LFPs with a relatively flat power spectrum. As CV increases, spiking activity becomes more synchronized, and the power spectrum of the LFP displays distinct peaks at specific frequencies. At high CV, spiking activity is highly synchronized, and the LFP power spectrum is dominated by a single low-frequency peak.We have shown that as CV increases, Shannon entropy of the LFP decreases while statistical complexity increases. Therefore, these quantifiers could potentially serve as markers of cortical state. Notably, our findings are qualitatively similar across varying numbers of possible LFP states and are not merely a consequence of finite sampling fluctuations. Interestingly, at very high CV, the complexity of the LFP reaches elevated values in the complexity-entropy ($C-H$) plane, suggesting that LFPs dominated by low-frequency peaks are more complex than those with a strong presence of higher frequency bands. This observation indicates that future studies should explore the relationship between statistical complexity, spectral composition, and coherence among signal phases to gain a deeper understanding of movements within the $C-H$ plane.

These results extend previous findings that have shown that the statistical complexity is a sensitive measure of cortical dynamics at the spiking level (LOTFI et al., 2021), where a maximum in complexity was observed in windows of mid-range CV, alongside low complexity for both high and low CV states. Our findings differ significantly; since low entropy states were never present when analyzing the information quantifiers of the LFP. While high CV windows, in

the context of firing rates signals exhibited low complexity, the LFP signals presented maximum complexity in this case. In the case of firing rates, high CV is characterized by the signal being close to zero for most of the time, punctuated by synchronized bursts. These prolonged periods of minimal activity result in very few permutations in the probability distribution, leading to low complexity. Conversely, for LFP signals at high CV, long slow waves co-occur with the high-frequency bursts of spikes, yielding higher complexity. However, further research into the coherence between these frequency bands is necessary to fully understand the observed maximum complexity in high CV windows.

Recording local field potentials (LFP) using silicon probes allows us to explore electrical events across all cortical layers, not just the deeper ones. This work leverages advancements in recording from large neuronal populations to quantify statistical complexity and entropy throughout the detailed laminar structure of the primary visual cortex (V1) (SAKATA; HARRIS, 2009; SENZAI; FERNANDEZ-RUIZ; BUSáKI, 2019). Our findings reveal that statistical complexity is sensitive to depth within V1, peaking in mid-layer 5, while entropy reaches its minimum at this depth as the coefficient of variation (CV) increases. This is particularly interesting, as it underscores the significance of layer 5, which contains a greater density of branched pyramidal neurons (SENZAI; FERNANDEZ-RUIZ; BUSáKI, 2019). The maximization of complexity in this specific layer was unexpected, given that layers $2/3$ are usually regarded as the critical layers in processing sensory information and is the layer 4 that receives and convey signals from the lateral geniculate nucleus of the thalamus to other layers. Layer 5 is characterized by larger pyramidal cells whose dendrites extend through all six layers. Thus, the maximum complexity observed in the LFP within this layer may reflect the integration of synaptic effects at the soma of these cells. Since this peak in complexity becomes evident only as CV increases, future studies could leverage this relationship to investigate connections between behavior and the visual cortex layers. Different behaviors may be associated with varying levels of CV, which could further elucidate the relationship between neuronal morphology and LFP dynamics.

Finally, we found that the statistical complexity of local field potentials (LFP) in mice varies significantly across different behavioral states: non-rapid eye movement (NREM) sleep, rapid eye movement (REM) sleep, and the awake state. Specifically, complexity is lowest during the awake state, intermediate during REM sleep, and highest during NREM sleep. The distinction between the complexity of the awake and REM states is particularly noteworthy, given that these behavioral states have been reported to exhibit similar LFP patterns (DESTEXHE; CONTRERAS; STERIADE, 1999). Notably, this difference was observed only in complexity, as

the entropy values presented overlapping error bars. Our findings regarding statistical complexity in mouse LFPs align with previous studies analyzing sleep stages in EEG data from humans (MATEOS; GóMEZ-RAMíREZ; ROSSO, 2021). These results open new avenues for applying information theory quantifiers to LFP data, offering valuable insights into cortical and behavioral states.

Overall, our results hold significant relevance for the field and were published as a PRE article (JUNGMANN et al., 2024). We established consistent relationships between local field potential (LFP) signals and spiking activity through information quantifiers, a connection not previously documented in the literature. Additionally, we identified anatomical differences in the LFP that emerged naturally when applying these quantifiers under varying levels of spiking variability. Moreover, this study confirmed that statistical complexity can serve as a marker for behavioral states at the intracranial recording level, a capability that has only been previously demonstrated using EEG recordings.

BIBLIOGRAPHY

BANDT, C.; POMPE, B. Permutation entropy: A natural complexity measure for time series. *Phys. Rev. Lett.*, v. 88, p. 174102, 2002.

BUTTERWORTH, S. On the theory of filter amplifiers. *Experimental Wireless and the Wireless Engineer*, v. 7, p. 536–541, 1930.

BUZSÁKI, G.; ANASTASSIOU, C. A.; KOCH, C. The origin of extracellular fields and currents–EEG, ECoG, LFP and spikes. *Nature Review Neuroscience*, Springer Science and Business Media LLC, v. 13, n. 6, p. 407–420, may 2012.

CHAITIN, G. J. Algorithmic information theory. *IBM Journal of Research and Development*, v. 21, n. 4, p. 350–359, 1977.

CRUTCHFIELD, J. P.; YOUNG, K. Inferring statistical complexity. *Phys. Rev. Lett.*, American Physical Society, v. 63, p. 105–108, Jul 1989. Available at: <https://link.aps.org/doi/10.1103/PhysRevLett.63.105>.

CSICSVARI, J.; HENZE, D. A.; JAMIESON, B.; HARRIS, K. D.; SIROTA, A.; BARTHÓ, P.; WISE, K. D.; BUZSÁKI, G. Massively parallel recording of unit and local field potential with silicon-based electrodes. *J. Neurophysiol.*, journals.physiology.org, v. 90, n. 2, p. 1314–1323, aug 2003.

DESTEXHE, A.; CONTRERAS, D.; STERIADE, M. Spatiotemporal analysis of local field potentials and unit discharges in cat cerebral cortex during natural wake and sleep states. *Journal of Neuroscience*, Society for Neuroscience, v. 19, n. 11, p. 4595–4608, 1999. ISSN 0270-6474.

EINEVOLL, G. T.; KAYSER, C.; LOGOTHETIS, N. K.; PANZERI, S. Modelling and analysis of local field potentials for studying the function of cortical circuits. *Nat. Rev. Neurosci.*, v. 14, n. 11, p. 770–785, nov 2013.

FONTENELE, A. J.; VASCONCELOS, N. A. P. de; FELICIANO, T.; AGUIAR, L. A. A.; SOARES-CUNHA, C.; COIMBRA, B.; PORTA, L. D.; RIBEIRO, S.; RODRIGUES, A. J. a.; SOUSA, N.; CARELLI, P. V.; COPELLI, M. Criticality between cortical states. *Phys. Rev. Lett.*, v. 122, p. 208101, 2019.

GERVASONI, D.; LIN, S.-C.; RIBEIRO, S.; SOARES, E. S.; PANTOJA, J.; NICOLELIS, M. A. L. Global forebrain dynamics predict rat behavioral states and their transitions. *Journal of Neuroscience*, Soc Neuroscience, v. 24, n. 49, p. 11137–11147, dec 2004.

GUISANDE, N.; NUNZIO, M. P. di; MARTINEZ, N.; ROSSO, O. A.; MONTANI, F. Chaotic dynamics of the hénon map and neuronal input–output: A comparison with neurophysiological data. *Chaos: An Interdisciplinary Journal of Nonlinear Science*, v. 33, n. 4, p. 043111, Apr 2023. ISSN 1054-1500.

HAHN, G.; PONCE-ALVAREZ, A.; MONIER, C.; BENVENUTI, G.; KUMAR, A.; CHAVANE, F.; DECO, G.; FRéGNAC, Y. Spontaneous cortical activity is transiently poised close to criticality. *PLOS Computational Biology*, Public Library of Science, v. 13, n. 5, p. 1–29, 05 2017.

HARRIS, K. D.; THIELE, A. Cortical state and attention. *Nature Reviews Neuroscience*, v. 12, n. 9, p. 509–523, Sep 2011.

HENRIE, J. A.; SHAPLEY, R. Lfp power spectra in v1 cortex: the graded effect of stimulus contrast. *Journal of neurophysiology*, American Physiological Society, v. 94, n. 1, p. 479–490, 2005.

HERRERAS, O. Local field potentials: Myths and misunderstandings. *Frontiers in Neural Circuits*, v. 10, 2016. ISSN 1662-5110.

JORDAN, D.; STOCKMANNS, G.; KOCHS, E. F.; PILGE, S.; SCHNEIDER, G. Electroencephalographic order pattern analysis for the separation of consciousness and unconsciousness: An analysis of approximate entropy, permutation entropy, recurrence rate, and phase coupling of order recurrence plots. *Anesthesiology*, v. 109, n. 6, p. 1014–1022, 12 2008. ISSN 0003-3022. Available at: <https://doi.org/10.1097/ALN.0b013e31818d6c55>.

JUN, J. J.; STEINMETZ, N. A.; SIEGLE, J. H.; DENMAN, D. J.; BAUZA, M.; BARBARITS, B.; LEE, A. K.; ANASTASSIOU, C. A.; ANDREI, A.; AYDIN, Ç.; BARBIC, M.; BLANCHE, T. J.; BONIN, V.; COUTO, J.; DUTTA, B.; GRATIY, S. L.; GUTNISKY, D. A.; HÄUSSER, M.; KARSH, B.; LEDOCHOWITSCH, P.; LOPEZ, C. M.; MITELUT, C.; MUSA, S.; OKUN, M.; PACHITARIU, M.; PUTZEYS, J.; RICH, P. D.; ROSSANT, C.; SUN, W.-L.; SVOBODA, K.; CARANDINI, M.; HARRIS, K. D.; KOCH, C.; O'KEEFE, J.; HARRIS, T. D. Fully integrated silicon probes for high-density recording of neural activity. *Nature*, v. 551, n. 7679, p. 232–236, Nov 2017. ISSN 1476-4687.

JUNGMANN, R. M.; FELICIANO, T.; AGUIAR, L. A. A.; SOARES-CUNHA, C.; COIMBRA, B.; RODRIGUES, A. J. a.; COPELLI, M.; MATIAS, F. S.; VASCONCELOS, N. A. P. de; CARELLI, P. V. State-dependent complexity of the local field potential in the primary visual cortex. *Phys. Rev. E*, American Physical Society, v. 110, p. 014402, Jul 2024.

KAJIKAWA, Y.; SCHROEDER, C. E. How local is the local field potential? *Neuron*, Elsevier, v. 72, n. 5, p. 847–858, Dec 2011. ISSN 0896-6273.

KANDEL, E. R. *Principles of Neural Science*. [S.l.]: McGraw Hill Professional, 2013.

KASS, R. E.; KELLY, R. C.; LOH, W.-L. Assessment of synchrony in multiple neural spike trains using loglinear point process models. *The Annals of Applied Statistics*, Institute of Mathematical Statistics, v. 5, n. 2B, p. 1262 – 1292, 2011.

KATZNER, S.; NAUHAUS, I.; BENUCCI, A.; BONIN, V.; RINGACH, D. L.; CARANDINI, M. Local origin of field potentials in visual cortex. *Neuron*, v. 61, n. 1, p. 35–41, jan 2009.

KINOUCHI, O.; COPELLI, M. Optimal dynamical range of excitable networks at criticality. *Nature Physics*, v. 2, n. 5, p. 348–351, May 2006. ISSN 1745-2481.

KLIMESCH, W. Alpha-band oscillations, attention, and controlled access to stored information. *Trends in Cognitive Sciences*, v. 16, n. 12, p. 606–617, 2012. ISSN 1364-6613.

KOLMOGOROV, A. N. Three approaches to the definition of the concept "quantity of information". *Probl. Peredachi Inf.*, p. 3–11, 1965.

LAMBERTI, P. W.; MARTíN, M. T.; PLASTINO, A.; ROSSO, O. A. Intensive entropic non-triviality measure. *Physica A: Statistical Mechanics and its Applications*, v. 334, n. 1, p. 119–131, 2004. ISSN 0378-4371.

LINDÉN, H.; TETZLAFF, T.; POTJANS, T. C.; PETTERSEN, K. H.; GRÜN, S.; DIESMANN, M.; EINEVOLL, G. T. Modeling the spatial reach of the lfp. *Neuron*, Elsevier, v. 72, n. 5, p. 859–872, Dec 2011. ISSN 0896-6273.

LIU, T. T.; FU, J. Z.; CHAI, Y.; JAPEE, S.; CHEN, G.; UNGERLEIDER, L. G.; MERRIAM, E. P. Layer-specific, retinotopically-diffuse modulation in human visual cortex in response to viewing emotionally expressive faces. *Nature Communication*, nature.com, v. 13, n. 1, p. 6302, oct 2022.

LOTFI, N.; FELICIANO, T.; AGUIAR, L. A. A.; SILVA, T. P. L.; CARVALHO, T. T. A.; ROSSO, O. A.; COPELLI, M.; MATIAS, F. S.; CARELLI, P. V. Statistical complexity is maximized close to criticality in cortical dynamics. *Phys. Rev. E*, v. 103, p. 012415, 2021.

LOTFI, N.; FONTENELE, A. J.; FELICIANO, T.; AGUIAR, L. A. A.; VASCONCELOS, N. A. P. de; SOARES-CUNHA, C.; COIMBRA, B.; RODRIGUES, A. J. a.; SOUSA, N.; COPELLI, M.; CARELLI, P. V. Signatures of brain criticality unveiled by maximum entropy analysis across cortical states. *Phys. Rev. E*, American Physical Society, v. 102, p. 012408, Jul 2020.

LUCAS, H.; BRESSLER, S.; MATIAS, F.; ROSSO, O. A. A symbolic information approach to characterize response-related differences in cortical activity during a go/no-go task. *Nonlinear Dyn*, v. 104, p. 4401–4411, 2021.

LUISE, R. D.; BARAVALLE, R.; ROSSO, O. A.; MONTANI, F. Network configurations of pain: an efficiency characterization of information transmission. *The European Physical Journal B*, v. 94, n. 1, p. 34, Jan 2021. ISSN 1434-6036.

LóPEZ-RUIZ, R.; MANCINI, H.; CALBET, X. A statistical measure of complexity. *Physics Letters A*, v. 209, n. 5, p. 321–326, 1995. ISSN 0375-9601.

MARTIN, M.; PLASTINO, A.; ROSSO, O. Generalized statistical complexity measures: Geometrical and analytical properties. *Physica A: Statistical Mechanics and its Applications*, v. 369, p. 439–462, 2006.

MATEOS, D.; DIAZ, J. M.; LAMBERTI, P. W. Permutation entropy applied to the characterization of the clinical evolution of epileptic patients under pharmacologicaltreatment. *Entropy*, v. 16, n. 11, p. 5668–5676, 2014. ISSN 1099-4300. Available at: <https://www.mdpi.com/1099-4300/16/11/5668>.

MATEOS, D. M.; GóMEZ-RAMíREZ, J.; ROSSO, O. A. Using time causal quantifiers to characterize sleep stages. *Chaos, Solitons & Fractals*, v. 146, p. 110798, 2021. ISSN 0960-0779.

MCGINLEY, M. J.; VINCK, M.; REIMER, J.; BATISTA-BRITO, R.; ZAGHA, E.; CADWELL, C. R.; TOLIAS, A. S.; CARDIN, J. A.; MCCORMICK, D. Waking state: Rapid variations modulate neural and behavioral responses. *Neuron*, v. 87, n. 6, p. 1143–1161, sep 2015.

MENDOZA-RUIZ, J.; ALONSO-MALAVER, C. E.; VALDERRAMA, M.; ROSSO, O. A.; MARTINEZ, J. H. Dynamics in cortical activity revealed by resting-state meg rhythms. *Chaos: An Interdisciplinary Journal of Nonlinear Science*, v. 30, n. 12, p. 123138, 12 2020. ISSN 1054-1500.

MONTANI, F.; BARAVALLE, R.; MONTANGIE, L.; ROSSO, O. A. Causal information quantification of prominent dynamical features of biological neurons. *Philosophical Transactions of the Royal Society A: Mathematical, Physical and Engineering Sciences*, v. 373, n. 2056, p. 20150109, 2015.

MONTANI, F.; DELEGLISE, E. B.; ROSSO, O. A. Efficiency characterization of a large neuronal network: A causal information approach. *Physica A: Statistical Mechanics and its Applications*, v. 401, p. 58–70, 2014. ISSN 0378-4371.

MONTANI, F.; ROSSO, O. A.; MATIAS, F. S.; BRESSLER, S. L.; MIRASSO, C. R. A symbolic information approach to determine anticipated and delayed synchronization in neuronal circuit models. *Philosophical Transactions of the Royal Society A: Mathematical, Physical and Engineering Sciences*, v. 373, n. 2056, p. 20150110, 2015.

NICKLAS, W.; BANEUX, P.; BOOT, R.; DECELLE, T.; DEENY, A. A.; FUMANELLI, M.; ILLGEN-WILCKE, B. Recommendations for the health monitoring of rodent and rabbit colonies in breeding and experimental units. *Laboratory Animals*, v. 36, n. 1, p. 20–42, 2002.

NICOLELIS, M. A. L.; DIMITROV, D.; CARMENA, J. M.; CRIST, R.; LEHEW, G.; KRALIK, J. D.; WISE, S. P. Chronic, multisite, multielectrode recordings in macaque monkeys. *Proc. Natl. Acad. Sci. U. S. A.*, National Acad Sciences, v. 100, n. 19, p. 11041–11046, sep 2003.

PAXINOS, G.; WATSON, C. *The Rat Brain in Stereotaxic Coordinates*. [S.l.]: Elsevier, 2016.

PESARAN, B.; VINCK, M.; EINEVOLL, G. T.; SIROTA, A.; FRIES, P.; SIEGEL, M.; TRUCCOLO, W.; SCHROEDER, C. E.; SRINIVASAN, R. Investigating large-scale brain dynamics using field potential recordings: analysis and interpretation. *Nat Neurosci*, v. 21, n. 7, p. 903–919, jun 2018.

PETRANTONAKIS, P. C.; POIRAZI, P. A simple method to simultaneously detect and identify spikes from raw extracellular recordings. *Frontiers in Neuroscience*, v. 9, p. 452, 2015.

RENART, A.; ROCHA, J. D. L.; BARTHO, P.; HOLLENDER, L.; PARGA, N.; REYES, A.; HARRIS, K. D. The asynchronous state in cortical circuits. *Science*, v. 327, n. 5965, p. 587–590, 2010.

RIBEIRO, T. L.; COPELLI, M.; CAIXETA, F.; BELCHIOR, H.; CHIALVO, D. R.; NICOLELIS, M. A. L.; RIBEIRO, S. Spike avalanches exhibit universal dynamics across the sleep-wake cycle. *PLoS One*, journals.plos.org, v. 5, n. 11, p. e14129, nov 2010.

RIMEHAUG, A. E.; STASIK, A. J.; HAGEN, E.; BILLEH, Y. N.; SIEGLE, J. H.; DAI, K.; OLSEN, S. R.; KOCH, C.; EINEVOLL, G. T.; ARKHIPOV, A. Uncovering circuit mechanisms of current sinks and sources with biophysical simulations of primary visual cortex. *eLife*, eLife Sciences Publications, Ltd, v. 12, p. e87169, jul 2023. ISSN 2050-084X.

RINGACH, D. L. Spontaneous and driven cortical activity: implications for computation. *Curr. Opin. Neurobiol.*, v. 19, n. 4, p. 439–444, aug 2009.

ROSSO, O.; MARTIN, M.; FIGLIOLA, A.; KELLER, K.; PLASTINO, A. Eeg analysis using wavelet-based information tools. *Journal of Neuroscience Methods*, v. 153, n. 2, p. 163–182, 2006.

ROSSO, O. A.; LARRONDO, H. A.; MARTIN, M. T.; PLASTINO, A.; FUENTES, M. A. Distinguishing noise from chaos. *Phys. Rev. Lett.*, American Physical Society, v. 99, p. 154102, Oct 2007.

SAKATA, S.; HARRIS, K. D. Laminar structure of spontaneous and sensory-evoked population activity in auditory cortex. *Neuron*, cell.com, v. 64, n. 3, p. 404–418, nov 2009.

SANCHO, L. e. a. Glia as sculptors of synaptic plasticity. *Neuroscience research*, v. 167, p. 17–29, 2021.

SCHÖLVINCK, M. L.; SALEEM, A. B.; BENUCCI, A.; HARRIS, K. D.; CARANDINI, M. Cortical state determines global variability and correlations in visual cortex. *Journal of Neuroscience*, Society for Neuroscience, v. 35, n. 1, p. 170–178, 2015. ISSN 0270-6474.

SENZAI, Y.; FERNANDEZ-RUIZ, A.; BUSáKI, G. Layer-specific physiological features and interlaminar interactions in the primary visual cortex of the mouse. *Neuron*, v. 101, p. 500–513, 2019.

SHADLEN, M. N.; NEWSOME, W. T. The variable discharge of cortical neurons: implications for connectivity, computation, and information coding. *Journal of neuroscience*, v. 18, n. 10, p. 3870–3896, 1998.

SHAI, A. S.; ANASTASSIOU, C. A.; LARKUM, M. E.; KOCH, C. Physiology of layer 5 pyramidal neurons in mouse primary visual cortex: coincidence detection through bursting. *PLoS Computational Biology*, v. 11, n. 3, p. e1004090, mar 2015.

SHANNON, C.; WEAVER, W. *The Mathematical Theory of Communication*. [S.l.]: University of Illinois Press, Champaign, IL, 1949.

SIEGLE, J. H.; LÓPEZ, A. C.; PATEL, Y. A.; ABRAMOV, K.; OHAYON, S.; VOIGTS, J. Open ephys: an open-source, plugin-based platform for multichannel electrophysiology. *Journal of neural engineering*, IOP Publishing, v. 14, n. 4, p. 045003, 2017.

SPROTT, J. C. *Chaos and Time-Series Analysis*. [S.l.]: Oxford University Press, 2003.

STEVENSON, I. H.; KORDING, K. P. How advances in neural recording affect data analysis. *Nature Neuroscience*, v. 14, n. 2, p. 139–142, Feb 2011. ISSN 1546-1726.

SUMMERFIELD, C.; JACK, A. I.; BURGESS, A. P. Induced gamma activity is associated with conscious awareness of pattern masked nouns. *International Journal of Psychophysiology*, v. 44, n. 2, p. 93–100, 2002. ISSN 0167-8760.

TSODYKS, M.; KENET, T.; GRINVALD, A.; ARIELI, A. Linking spontaneous activity of single cortical neurons and the underlying functional architecture. *Science*, v. 286, n. 5446, p. 1943–1946, 1999.

VASCONCELOS, N. A. P. de; SOARES-CUNHA, C.; RODRIGUES, A. J.; RIBEIRO, S.; SOUSA, N. Coupled variability in primary sensory areas and the hippocampus during spontaneous activity. *Scientific Reports*, v. 7, n. 1, p. 46077, Apr 2017. ISSN 2045-2322.

VOGELS, T. P.; ABBOTT, L. F. Signal propagation and logic gating in networks of integrate-and- fire neurons. *Journal of Neuroscience*, Society for Neuroscience, v. 25, n. 46, p. 10786–10795, 2005. ISSN 0270-6474.

VYAZOVSKIY, V.; OLCESE, U.; TONONI, G. Investigating sleep homeostasis with extracellular recording of multiunit activity from the neocortex in freely behaving rats. *Neuromethods*, v. 67, p. 237–258, 12 2011.

XIONG, H.; SHANG, P.; HE, J.; ZHANG, Y. Complexity and information measures in planar characterization of chaos and noise. *Nonlinear Dynamics*, v. 100, n. 2, p. 1673–1687, Apr 2020. ISSN 1573-269X.

ZHANG, H.; XIE, J.; LI, Y.; LIU, H.; LIU, C.; KAN, D.; GENG, X.; WEI, S. Levodopa affects spike and local field synchronisation in the pedunculopontine nucleus of a rat model of parkinson's disease. *Aging*, Impact Journals, LLC, v. 13, n. 5, p. 7314–7329, 2021. ISSN 1945-4589.

ZHU, L.; CUI, G.; CAO, J.; CICHOCKI, A.; ZHANG, J.; ZHOU, C. A hybrid system for distinguishing between brain death and coma using diverse eeg features. *Sensors*, v. 19, n. 6, 2019. ISSN 1424-8220. Available at: <https://www.mdpi.com/1424-8220/19/6/1342>.

ZUNINO, L.; SORIANO, M. C.; ROSSO, O. A. Distinguishing chaotic and stochastic dynamics from time series by using a multiscale symbolic approach. *Phys. Rev. E*, American Physical Society, v. 86, p. 046210, Oct 2012.